

Sec14L6 is a phosphoinositide transporter that regulates phosphoinositide homeostasis and biogenesis of lipid droplets

Received: 13 June 2025

Accepted: 17 October 2025

Published online: 26 November 2025

 Check for updatesTiantian Zhou^{1,6}, Juan Xiong^{2,6}, Xuewen Hu^{1,6}, Yuanjiao Du³, Anbing Shi^{1,4}, Weiping Chang³, Jichao Qin⁵, Lin Deng³ & Wei-Ke Ji^{1,3,4} ✉

Lipid droplets (LDs) are evolutionarily conserved organelles essential for cellular metabolism. They form and grow at the endoplasmic reticulum (ER), requiring lipid transfer between these compartments, yet the underlying molecular mechanisms remain elusive. We identify Sec14L6, a unique Sec14 family member, as a lipid transporter regulating phosphoinositide (PIP) homeostasis and LD biogenesis, promoting adipogenic differentiation of mesenchymal stem cells. Sec14L6 directly binds the LD biogenesis factor ACSL3, which facilitates the association of Sec14L6 with LD surface. Furthermore, the ER membrane protein PGRMC1 recruits Sec14L6 to the ER. Targeted lipidomics revealed profound PIP dysregulation in Sec14L6-KO cells: LDs accumulated phosphoinositide-4-phosphate (PI4P) and PI(4,5)P₂, while these PIPs were reduced within the ER. In vitro assays demonstrated that Sec14L6 transports PI4P and PI(4,5)P₂. Sec14L6 knockout significantly impaired LD formation; this defect was rescued by wild-type Sec14L6, but not by lipid-transfer-deficient mutants. Our study reveals an essential role for Sec14L6 in PIP homeostasis and promotes LD biogenesis through lipid transfer between the ER and LDs.

Lipid droplets (LDs) are storage organelles that play central roles in lipid and energy homeostasis^{1,2}. They store neutral lipids in a hydrophobic core of triacylglycerol and cholesteryl esters surrounded by a phospholipid monolayer associated with proteins^{3,4}. LDs play an important role in cellular adaptation to energy fluctuations and are also involved in other cellular functions, such as protein quality control, regulation of gene transcription, lipid and membrane traffic, and inflammatory responses^{5,6}.

The biogenesis of LDs occurs in the endoplasmic reticulum (ER) in response to an excess of neutral lipids following the biosynthesis and

deposition of neutral lipids in the hydrophobic region of the bilayer⁷. These neutral lipids condense and form the core of a nascent LD, which grows and then buds off the ER to become a mature LD⁸. During LD biogenesis, LDs acquire surface phospholipids from the ER to enable ongoing phospholipid monolayer membrane expansion and growth. During the initial phase of their life, the monolayers of nascent LDs are contiguous with the cytosolic leaflet of the ER membrane⁹, several key components of which have been identified, including Seipin^{10–12}, DGATs¹³, ACSL3¹⁴, and FIT2¹⁵. Next, LDs bud toward the cytosol and detach from the ER to form mature LDs, which continue to maintain

¹Department of Biochemistry and Molecular Biology, School of Basic Medicine, Tongji Medical College and State Key Laboratory for Diagnosis and Treatment of Severe Zoonotic infectious Diseases, Huazhong University of Science and Technology, Wuhan, China. ²Department of Anesthesiology and Pain Medicine, Hubei Key Laboratory of Geriatric Anesthesia and Perioperative Brain Health, and Wuhan Clinical Research Center for Geriatric Anesthesia, Tongji Hospital, Tongji Medical College, Huazhong University of Science and Technology, Wuhan, China. ³Shenzhen Bay Laboratory, Shenzhen, China. ⁴Cell Architecture Research Center, Huazhong University of Science and Technology, Wuhan, China. ⁵Department of Gastrointestinal Surgery, the First Affiliated Hospital, Zhejiang University School of Medicine, Hangzhou, Zhejiang, China. ⁶These authors contributed equally: Tiantian Zhou, Juan Xiong, Xuewen Hu.

✉ e-mail: Weike_Ji1985@163.com

physical contact with the ER through lipid transfer protein (LTP)¹⁶, such as ORPs¹⁷ and VPS13^{18,19}. It has been reported that this physical interaction promotes the supply of phospholipids for the growth of mature LDs from the ER²⁰. Notably, it has been shown that key enzymes involved in phospholipid and sterol biosynthesis can translocate to the LD surface for the local synthesis of lipids during mature LD growth²¹. However, the molecular basis of LD biogenesis remains incompletely understood, and little is known about whether and how lipid transfer occurs between the ER and LDs.

Sec14-like (Sec14L) proteins constitute an atypical subfamily of phosphoinositide transfer proteins (PITPs) that are conserved from yeast (Sec14p) to humans (Sec14L1-6)^{22,23}. Sec14L proteins feature a unique domain architecture that combines a CRAL-TRIO lipid-binding domain with a Golgi dynamic domain (GOLD), which is absent in yeast Sec14p. While yeast Sec14p functions primarily in vesicle trafficking, Sec14L homologs are conserved in plants²⁴ and play expanded roles in lipid signaling, stress adaptation, and developmental processes. For example, Arabidopsis PATL1 proteins regulate tolerance to abiotic stress and plant development, with the GOLD domain potentially mediating protein–protein or protein–membrane interactions critical for these functions. These plant studies underscore the evolutionary diversification of Sec14-related proteins and their adaptation to complex eukaryotic systems^{25,26}.

Sec14L proteins in humans are also involved in diverse physiological functions. For example, Sec14L2 has been reported to modulate cholesterol synthesis and hepatitis C virus replication^{27,28}. Meanwhile, in zebrafish, zSec14L3 (a homolog of human Sec14L2) regulates Wnt/Ca²⁺ signaling and zebrafish vasculogenesis^{29,30}. In addition, zSec14L3 promotes the conversion of phosphoinositide-4-phosphate (PI4P) to PI3P to control ER-mediated endosomal fission³¹. Emerging evidence links PITPs, such as yeast Pdr16 and Sfh3, to LD metabolism^{6,32–34}. However, the role of Sec14L proteins in LD dynamics has remained unclear. To bridge this gap, we demonstrated that Sec14L6 regulates phosphoinositide homeostasis and biogenesis of LDs, and is important for differentiation of adipose-derived mesenchymal stem cells. Sec14L6 directly interacts with ACSL3, which facilitates Sec14L6 targeting to LDs. We identify PGRMC1 as an adaptor that recruits Sec14L6 to the ER. Targeted lipidomics revealed profound dysregulation of PIP homeostasis: LDs from Sec14L6-KO cells exhibited aberrant accumulation of PI4P and PI(4,5)P₂, concomitant with a reduction of these PIPs within the ER compartment. In vitro assays demonstrate that Sec14L6 preferentially transports phosphoinositide-4-phosphate (PI4P) and PI(4,5)P₂. Sec14L6 knockout (KO) severely impaired LD formation, a defect rescued by wild-type Sec14L6 but not by lipid-transfer-deficient mutants. Our study identified Sec14L6 as a factor that regulates PIP homeostasis and biogenesis of LDs via lipid transfer between the ER and LDs.

Results

Lipid droplet formation is impaired in Sec14L6-depleted cells

To investigate whether Sec14L proteins are involved in LD dynamics, we performed a candidate RNAi screen. In this screening, HeLa cells were cultured in Earle's Balanced Salt Solution (EBSS) for -12 h to consume existing LDs, followed by stimulating nascent LD formation by the addition of oleic acid (OA) (EBSS-OA). Suppression of Sec14L proteins, including Sec14L1–L5, by small interfering RNAs (siRNAs) had no significant effect on the number or size of LDs compared with the control (Fig. 1a, top and middle; Fig. 1b, c & Supplementary Fig. 1a–e). In contrast, depletion of Sec14L6 by two independent siRNAs greatly reduced the number of LDs (Fig. 1a, bottom; Supplementary Fig. 1f, g), suggesting a role for Sec14L6 in LD formation.

To confirm that Sec14L6 plays a specific role in LD formation, we investigated its role under canonical LD induction conditions in which cells were cultured in lipoprotein-free medium followed by OA loading for -15 min, as previously reported¹¹. Sec14L6 depletion greatly

reduced the number of LDs under these conditions (Fig. 1d, e). The phenotype can be observed in other human cell lines such as Huh-7 and HepG2 (Supplementary Fig. 1h, i). Notably, Sec14L6 depletion did not dramatically affect the number of LDs under normal growth conditions (Fig. 1f, g), in which LD biogenesis was not strongly stimulated, suggesting that Sec14L6 plays a specific role in nascent LD formation.

We further confirmed the role for Sec14L6 in LD formation in CRISPR–Cas9-mediated Sec14L6-knockout HeLa cells (Sec14L6 KO; Supplementary Fig. 1j–m). Consistent with the above findings, LD formation was severely impaired in two independent Sec14L6-KO clones (KO-2 & -4), as evidenced by a substantial reduction in the abundance of LDs (Fig. 1h, i). We used the KO-2 clone for all following experiments unless otherwise indicated.

To further validate these results, we measured cellular triglyceride (TG) levels. Notably, siRNA-mediated depletion of Sec14L6 led to a modest reduction in cellular TG levels, comparable to the decrease observed upon depletion of known LD biogenesis factors such as Seipin and ACSL3 (Supplementary Fig. 1n). A similar mild decline in total TG levels was observed in two Sec14L6 KO clones (Supplementary Fig. 1o). Importantly, the reduction in TG was substantially greater in the LD fraction compared to the whole-cell lysate (Fig. 1j). In addition, an increase in TG concentration was observed in ER fractions from Sec14L6 KO cells (Supplementary Fig. 1p), which may account for the relatively modest overall reduction in cellular TG in Sec14L6 KO cells. The purity of the LD and ER fractions were confirmed (See results section 'Sec14L6 deficiency impaired PIP homeostasis of the ER and LD' and Supplementary Fig. 5f).

Since TG accumulation in the ER is tightly linked to maintenance of ER homeostasis³⁵, we investigated whether Sec14L6 deficiency triggers ER stress. Immunoblotting revealed upregulation of ER stress markers, including BiP and eIF2 α /p-eIF2 α (Supplementary Fig. 2a). This was further supported by an increased formation of ER whorls (marked by Sec61 β) (Supplementary Fig. 2b, c), a known hallmark of ER stress³⁶. These results indicate that Sec14L6 deficiency impairs ER homeostasis, leading to ER stress. Notably, this stress did not compromise cell viability, as measured by CCK8 assay (Supplementary Fig. 2d).

We next asked whether the reduced LD abundance in Sec14L6 KO cells resulted from accelerated turnover. Using the lipophagy reporter RFP-GFP-PLIN2³⁷, we found that serum starvation induced lipophagy efficiently; however, Sec14L6 loss did not significantly alter the LD turnover rate (Supplementary Fig. 2e, f). This suggests that Sec14L6 specifically regulates LD biogenesis rather than their degradation.

We next performed transmission electron microscopy (TEM) to examine the ultrastructural details of residual LDs in Sec14L6 KO HeLa cells. TEM micrographs revealed a slight reduction in LD size in Sec14L6-KO cells (Fig. 1k, l). Importantly, TEM confirmed that Sec14L6 KO resulted in a strong reduction in the number of LDs per cell compared with that in the control (Fig. 1k, m).

Next, we investigated the functional relationship of Seipin and a lipid transporter ORP5 (both known to regulate LD dynamics^{38,39}) with Sec14L6. Overexpression of GFP-Seipin (Supplementary Fig. 3a) or GFP-ORP5 (Supplementary Fig. 3b) failed to restore the LD defect in the Sec14L6-KO line (Supplementary Fig. 3c, d). Conversely, GFP-Sec14L6 did not ameliorate the LD phenotype in ORP5- or Seipin-depleted HeLa cells (Supplementary Fig. 3e–m), indicating non-redundant roles for these three proteins. This was further supported by the cumulative effect observed upon double suppression of Sec14L6 and ORP5, which resulted in fewer, larger (>1 μ m in diameter) LDs—a more severe phenotype than either single knockdown (Supplementary Fig. 3n–p). In addition, Sec14L6 overexpression had minimal impact on LD size or number in HeLa (Supplementary Fig. 3q, s, t) or in a mouse cell line AML-12 which lacks the Sec14L6 gene (Supplementary Fig. 3r–t), suggesting that while Sec14L6 facilitates LD formation, its overexpression alone is not sufficient to mediate LD biogenesis.

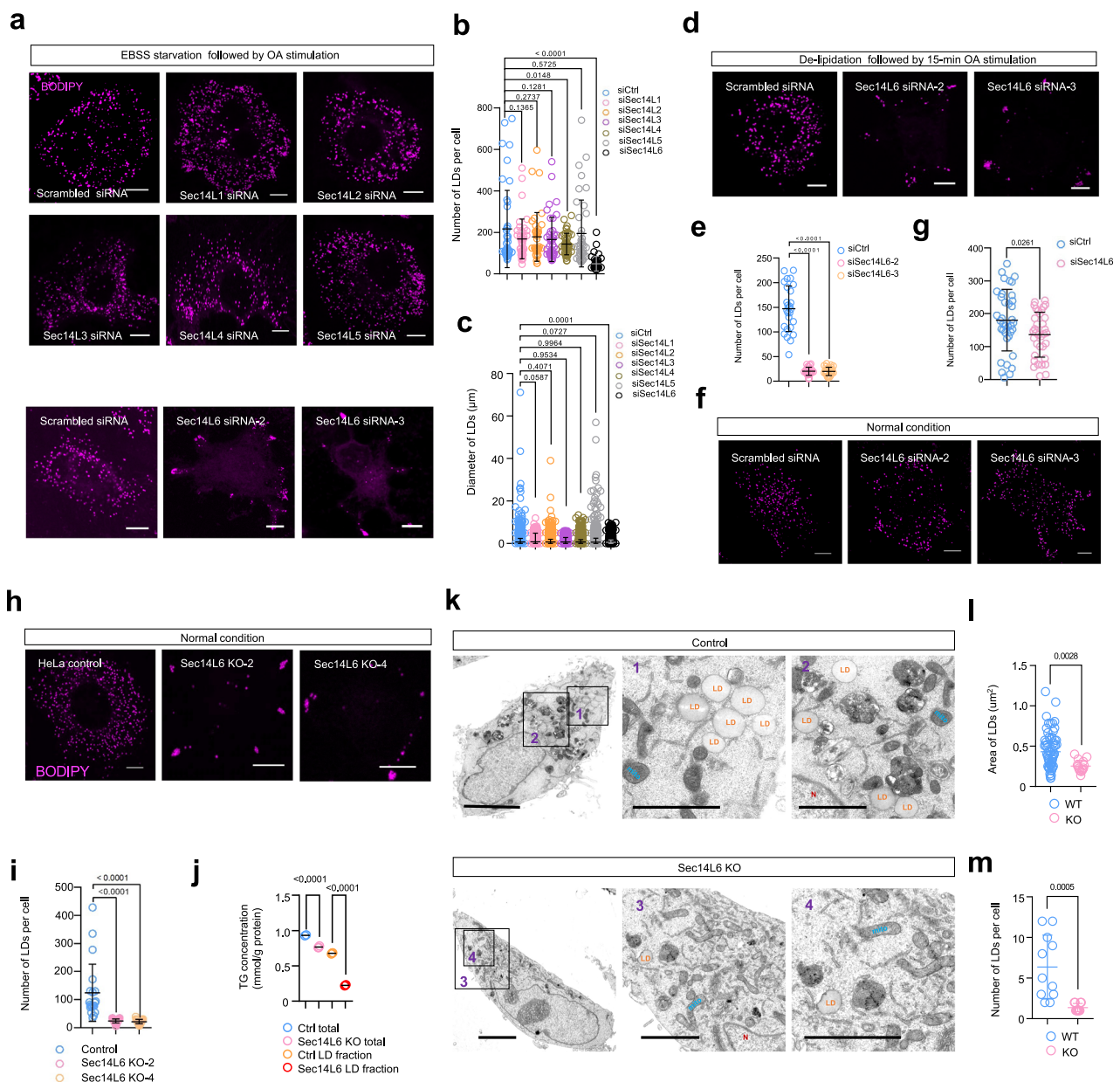
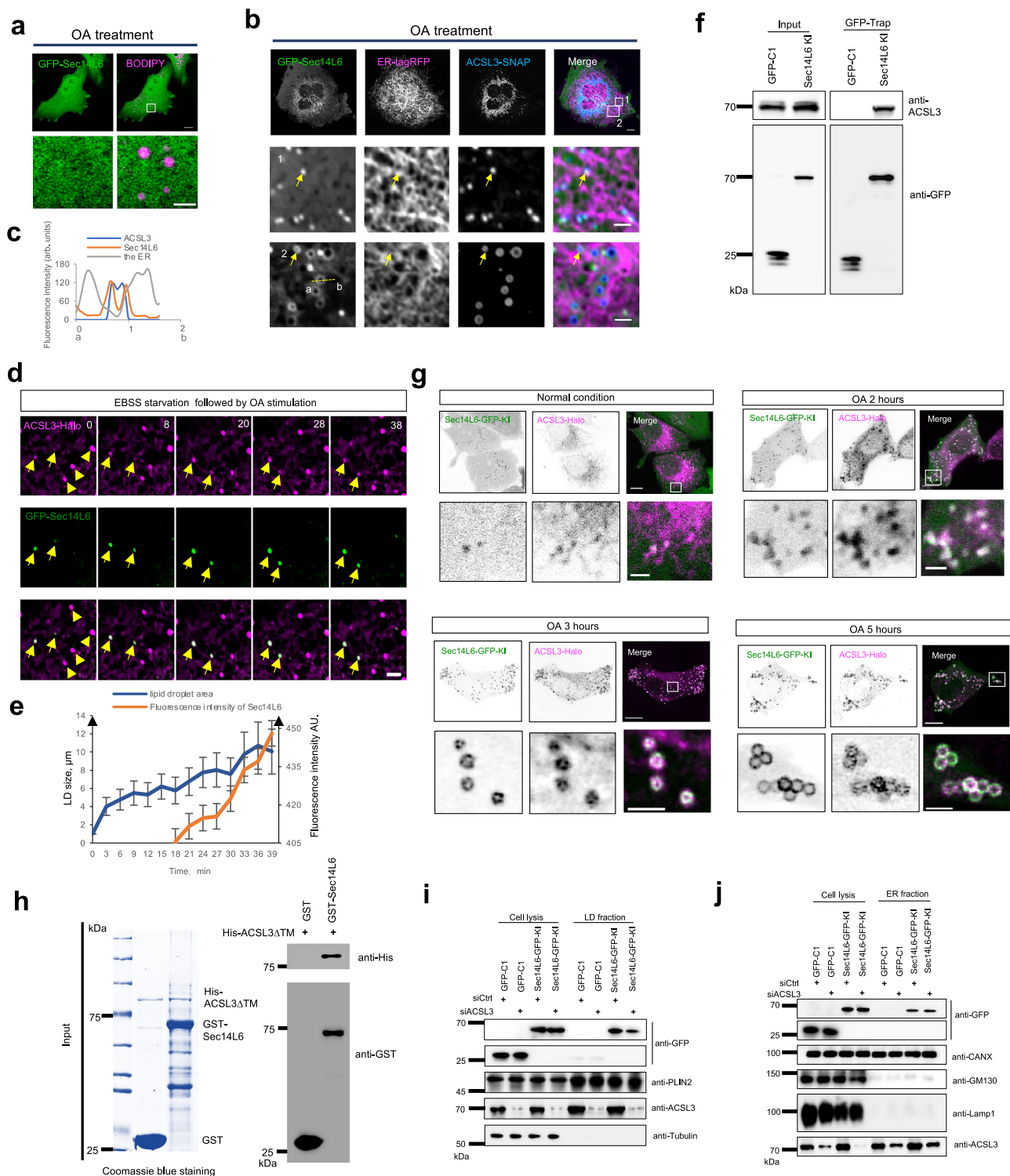


Fig. 1 | Depletion of Sec14L6 impairs the formation of LDs. **a** Representative images of live BODIPY-C12 558/568 (BODIPY; magenta)-labeled HeLa cells treated with scrambled or siRNAs targeting Sec14L1-6 upon EBSS-OA treatments. The number (**b**) or size (**c**) of LDs in cells as shown in (**a**) in more than 3 independent experiments with at least 40 cells quantified per group. Ordinary one-way ANOVA with Tukey's multiple comparisons test. Mean \pm SD. **d** Representative images of live BODIPY (magenta)-labeled HeLa cells treated with scrambled or siRNAs targeting Sec14L6 upon de-lipidation followed by -15-min OA treatment. **e** The number of LDs in cells as shown in (**d**) in 3 independent experiments with at least 21 cells quantified per group. Ordinary one-way ANOVA with Tukey's multiple comparisons test. Mean \pm SD. **f** Representative images of live BODIPY (magenta)-labeled HeLa cells treated with scrambled or siRNAs targeting Sec14L6 under normal culture condition. **g** LD number in cells as shown in (**f**) in 3 independent experiments

with at least 35 cells quantified per group. Two-tailed unpaired Student's *t* test. Mean \pm SD. **h** Representative images of live BODIPY (magenta)-labeled control or Sec14L6 KO HeLa cells under normal culture condition. **i** LD number in cells as shown in (**h**) in more than 3 independent experiments with at least 19 cells quantified per group. Ordinary one-way ANOVA with Tukey's multiple comparisons test. Mean \pm SD. **j** TG levels in whole cell lysate or LD fractions from control or Sec14L6 KO HeLa cells ($n = 3$). Measurements of TG were from 3 independent experiments. Two-tailed unpaired Student's *t* test. Mean \pm SD. **k** Representative TEM images of control or Sec14L6 KO HeLa cells under normal culture condition with insets. The LD size (**l**) and LD number per cell (**m**) as shown in (**k**) in 3 independent experiments with at least 11 cells quantified per group. Two-tailed unpaired Student's *t* test. Mean \pm SD. Scale bar, 10 μ m in the whole cell image. 5 μ m in the whole cell images and 2 μ m in the insets in (**k**).

ACSL3 facilitates the association of Sec14L6 with lipid droplets
To determine whether Sec14L6 localizes to LDs, we analyzed GFP-tagged Sec14L6 constructs. Both N-terminally tagged GFP-Sec14L6 (Fig. 2a) and C-terminally tagged Sec14L6-GFP (Supplementary Fig. 4a) exhibited diffuse cytosolic localization with no detectable membrane association under basal or OA-treated conditions. Interestingly, we found that ACSL3, an important factor in LD biogenesis¹⁴, facilitated

the recruitment of GFP-Sec14L6 to the surfaces of both small (middle panel) and large LDs (bottom panel) after OA stimulation (Fig. 2b). These small LDs marked with GFP-Sec14L6 appeared to be adjacent to the ER, likely representing ER-LD surfaces. In addition, GFP-Sec14L6 also decorated with large LDs not closely associating with the ER (Fig. 2c). These results suggest that ACSL3 facilitates the targeting of Sec14L6 to LDs.



Next, using time-lapse imaging, we tracked the process of nascent LD growth in live HeLa cells. GFP-Sec14L6 was colocalized with small LDs marked by ACSL3-Halo, and these small LDs grew as Sec14L6 puncta became larger (Fig. 2d, e; Supplementary Movie 1).

We then investigated whether Sec14L6 interacts with ACSL3. Our co-IP assays showed that GFP-Sec14L6 did indeed interact with endogenous ACSL3 (Supplementary Fig. 4b). To avoid potential artifacts of overexpression, we labeled endogenous Sec14L6 with monomeric superfolder GFP (sfGFP) at its C-terminus using CRISPR-Cas9 in HeLa cells (Sec14L6-GFP-KI) (Supplementary Fig. 4c–e). We chose to tag Sec14L6 at the C-terminus in the KI line for two reasons. First, the best

sgRNA for KI is located in this region (Supplementary Fig. 4c). Second, tagging at the C-terminus did not affect the localization of Sec14L6, its interactions with other proteins as identified in this study (Supplementary Fig. 4f, g), or its function in LD formation (See results section ‘Lipid transfer activity of Sec14L6 is required for LD biogenesis’). The Sec14L6–ACSL3 interaction was confirmed at the endogenous level by coIP assays in Sec14L6-GFP KI HeLa cells (Fig. 2f).

Notably, Sec14L6-GFP-KI was recruited to LDs labeled with ACSL3-mCh even without OA treatment, and the extent of recruitment to the LD surface was increased with the growth of LDs induced by OA stimulation for the indicated time (Fig. 2g).

Fig. 2 | ACSL3 facilitates the association of Sec14L6 with LDs. **a** Representative images of a live BODIPY (magenta)-labeled HeLa cell transiently transfected with GFP-Sec14L6 (green) under OA stimulation with an inset on the bottom from at least 3 independent experiments. **b** Representative images of a live HeLa cell transiently transfected with GFP-Sec14L6 (green), ER-tagRFP (magenta) and ACSL3-SNAP (blue) under OA stimulation (>6 h) with two insets on the bottom from at least 3 independent experiments. A yellow arrow denotes a Sec14L6-decorated LD. **c** Line-scan analysis of the bottom inset from (b). **d** Time-lapse montages of a HeLa cell transiently transfected with GFP-Sec14L6 (green) and ACSL3-mCh (magenta) with arrows denoting growing LDs from 3 independent experiments. **e** The correlation between LD diameter and GFP-Sec14L6 fluorescence intensity as in (d). **f** Representative GFP-Trap assays demonstrated interactions between endogenous Sec14L6-GFP-KI and endogenous ACSL3 from at least 3 independent experiments. **g** Representative images of live BODIPY-stained Sec14L6-GFP-KI (green) cells

transiently transfected with ACSL3-Halo (magenta) in absence or presence of OA loading for indicated time (2, 3 and 5 h) with insets on the bottom from at least 3 independent experiments. **h** GST pull-down assays showed that GST-Sec14L6 was pelleted with purified His-ACSL3- Δ TM in vitro from 3 independent experiments. The Coomassie blue staining of proteins used in the assay was shown on the left. **i** Membrane fractionation showing the level of Sec14L6-GFP-KI was reduced in LD fractions upon ACSL3 depletion under LD-induction condition as in Fig. 1d from 3 independent experiments. LD fractions from control and ACSL3-depleted cells were normalized to Plin2 levels. **j** Immunoblots showed the level of Sec14L6-GFP-KI in ER membrane fractions of either control or ACSL3-depleted cells using GFP vector as a negative control under LD-induction condition as in Fig. 1d from 3 independent experiments. ER fractions from control and ACSL3-depleted cells were normalized to Plin2 levels. Scale bar, 10 μ m in the whole cell images and 2 μ m in the insets in (a, b, d & g).

To investigate whether this Sec14L6–ACSL3 interaction occurs in a direct manner, we performed GST pull-down assays. His-tagged ACSL3 lacking its transmembrane domain (ACSL3- Δ TM) bound to GST-tagged Sec14L6 but not to the GST tag (Fig. 2h), indicating that Sec14L6 binds to ACSL3.

To further investigate whether ACSL3 is required for the localization of Sec14L6 to LDs, we performed membrane fractionation. siRNA-mediated depletion of ACSL3 reduced the amounts of endogenous Sec14L6-GFP-KI in LD fractions (Fig. 2i). In contrast, ACSL3 depletion did not substantially alter the level of Sec14L6-GFP-KI in ER fractions (Fig. 2j). Taken together, our results indicate that ACSL3 binds to Sec14L6 and promotes the association of Sec14L6 with LDs.

Molecular mechanism of the Sec14L6–ACSL3 interaction

Next, we investigated the mechanism underlying the interaction between Sec14L6 and ACSL3. Sec14L6 contains an N-terminal region (NT), a CRAL-TRIO domain, and a Golgi dynamics domain (GOLD) in its C-terminal region (CT) (Fig. 3a)²². Pull-down assays demonstrated that the CRAL-TRIO domain and the GOLD domain, but not the NT region, could bind to purified His-ACSL3- Δ TM. Notably, the CRAL-TRIO bound to His-ACSL3- Δ TM to a much higher extent than the GOLD domain did (Fig. 3b).

Consistent with these findings, live-cell imaging showed that the CRAL-TRIO domain, but not the NT or GOLD, colocalized with ACSL3 (Fig. 3c). In addition, deletion of the CRAL-TRIO domain, but not the NT or GOLD, abolished the colocalization between Sec14L6 and ACSL3 (Fig. 3d), suggesting that the CRAL-TRIO domain is responsible for binding to ACSL3 on the LD surface.

We next dissected the CRAL-TRIO domain to identify the region responsible for the interaction with ACSL3. We found that deletion of an α -helix (residues 160–185), a sheet (residues 186–192), or an α -helix (residues 193–249) partially abolished the interaction with endogenous ACSL3, whereas the deletion of other secondary structures in this domain had no such effect (Fig. 3e, f). This suggests that the region of the CRAL-TRIO domain containing the helix-sheet-helix is required for the interaction with ACSL3.

ACSL3 has a TM domain in the NT region, an AMP-binding domain, and a CT region (Fig. 3g). Deletion of the NT region of ACSL3 (with retention of the TM domain), but not the AMP-binding domain or the CT, abolished colocalization between ACSL3 and Sec14L6 (Fig. 3h), indicating that the NT region of ACSL3 is required to facilitate Sec14L6 recruitment to LDs.

Next, we investigated whether the interaction with Sec14L6 impacts ACSL3 activity. Overexpression of ACSL3 significantly increased the ACSL activity in cell lysates, validating the sensitivity of this assay. Expression of either WT Sec14L6, the CRAL-TRIO domain or Sec14L6- Δ CRAL-TRIO did not substantially affect the ACSL3 activity. In addition, Sec14L6 KO did not alter the ACSL activity either (Supplementary Fig. 4g). These results suggest that Sec14L6 regulates LD formation independently of ACSL3 activity.

Furthermore, GFP-Trap assays demonstrated multiple interactions between the domains of Sec14L6 and ACSL3, with the interaction between Sec14L6-CRAL-TRIO and ACSL3-NT being the most significant (Fig. 3i). Accordingly, GST pull-down assays demonstrated that GST-Sec14L6 could bind to His-ACSL3-NT- Δ TM and His-ACSL3-CT, albeit to a much lesser extent than for ACSL3- Δ TM. Notably, GST-Sec14L6- Δ CRAL-TRIO did not bind to purified ACSL3- Δ TM or its truncated forms (Fig. 3j).

Interestingly, we found that Sec14L6 could interact with itself (Supplementary Fig. 4h), which involved its CRAL-TRIO domain and the GOLD domain in the CT region of Sec14L6 (Supplementary Fig. 4i, j). Cross-linking mediated by disuccinimidyl suberate (DSS) promoted the oligomerization of Flag-Sec14L6 in HeLa cells in a dose-dependent manner (Supplementary Fig. 4k). These results suggest that the Sec14L6–ACSL3 interaction is mediated by multiple interactions between Sec14L6 oligomers and ACSL3. To test this, we performed coIP under DSS treatment, and found that ACSL3 was indeed pelleted with oligomeric Sec14L6 in a protein complex (Supplementary Fig. 4l), confirming that oligomeric Sec14L6 interacts with ACSL3.

The CRAL-TRIO domain of Sec14L6 targets LDs via an amphipathic helix

Surprisingly, unlike the full-length Sec14L6, the CRAL-TRIO domain was able to target LDs in the absence of ACSL3 (Fig. 4a). In addition, although ACSL3 was able to facilitate the association of full-length Sec14L6 with LDs, depletion of ACSL3 did not block LD localization of the CRAL-TRIO domain after OA loading (Fig. 4b, c), suggesting that the CRAL-TRIO domain of Sec14L6 is able to target LD independently of ACSL3.

The CRAL-TRIO domain of MOSPD2 has been shown to target LD via an amphipathic helix (AH)⁴⁰. We thus hypothesized that the CRAL-TRIO domain of Sec14L6 might target LD via the same mechanism. A segment in the CRAL-TRIO domain of Sec14L6 was predicted to fold as an AH (Fig. 4d, e). The AH is conserved in Sec14p and other Sec14L proteins, with the AH in Sec14L6 exhibiting the highest hydrophobic moment (Supplementary Fig. 4m). Mutation of a conserved residue (C135) on the hydrophobic side of this AH reduced the localization on LDs (Fig. 4f, g), indicating that the AH is required for the localization of the CRAL-TRIO domain to LD surface.

To further validate these results, we performed in vitro liposome pelleting assays (Fig. 4h). The His-tagged CRAL-TRIO domain of Sec14L6, but not His-Sec14L6- Δ CRAL-TRIO, could be substantially pelleted by sucrose-loaded liposomes (Fig. 4i), indicating that GST-CRAL-TRIO can target liposome membranes in vitro. In contrast, purified GST-Sec14L6 was barely associated with liposomes (Fig. 4j, k). Notably, the addition of purified His-ACSL3- Δ TM significantly enhanced the association of Sec14L6 with liposomes. The effect was mediated by ACSL3-NT, as the addition of His-ACSL3-NT- Δ TM, but not His-ACSL3-CT, promoted the targeting of GST-Sec14L6 to liposomes (Fig. 4k). Meanwhile, neither His-ACSL3- Δ TM nor the two truncations

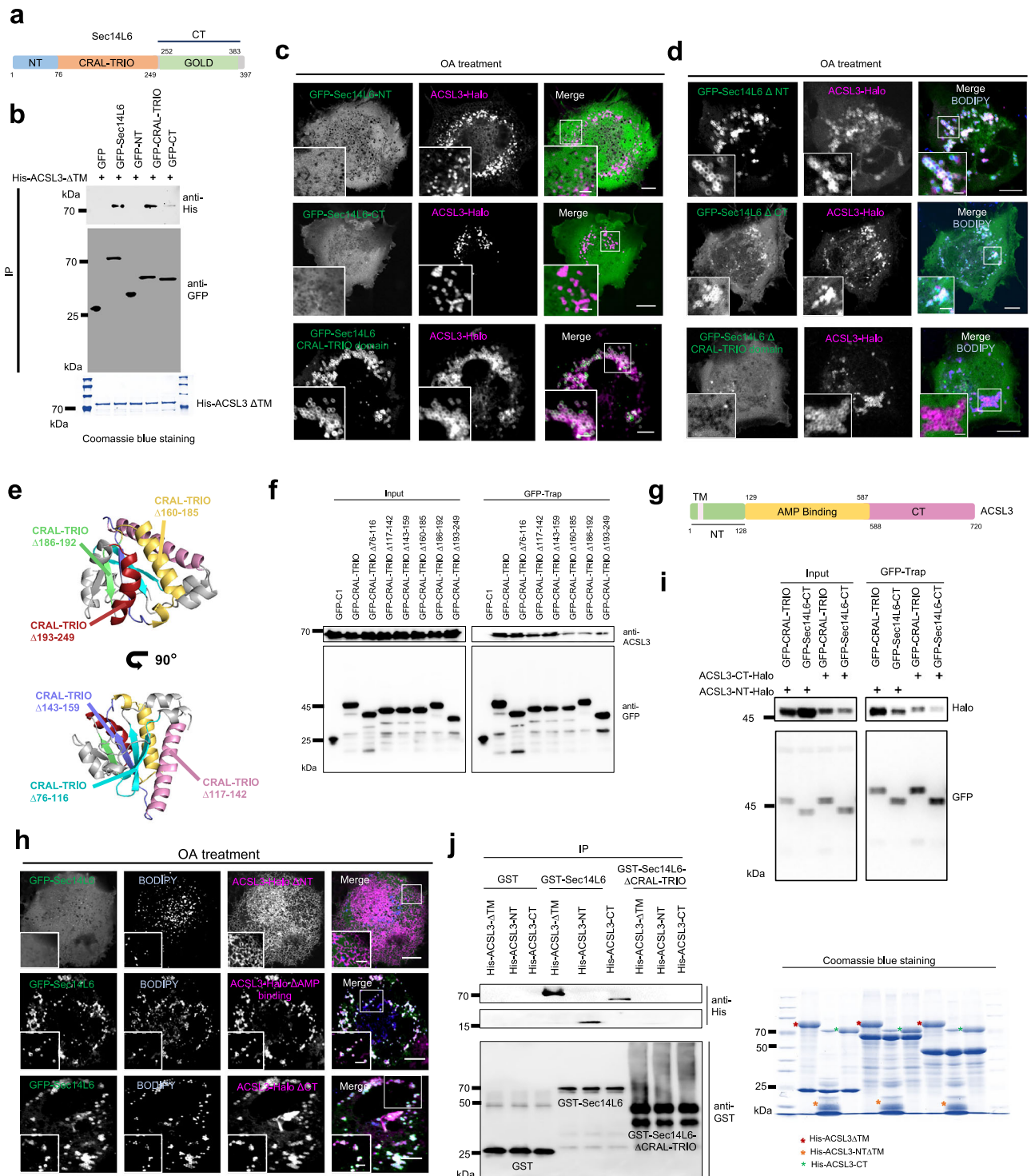
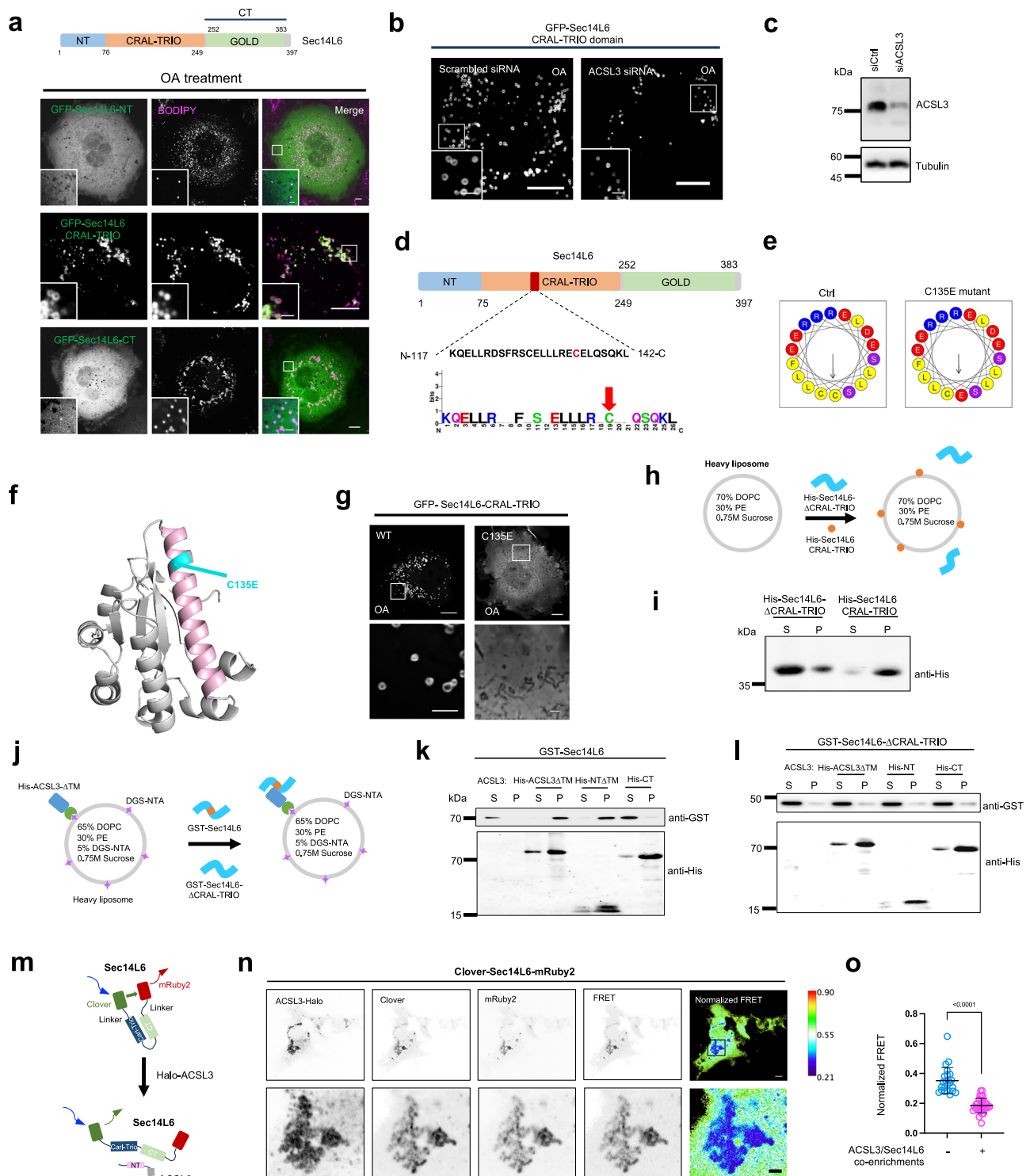


Fig. 3 | Molecular mechanism underlying the Sec14L6-ACSL3 interaction. **a** Domain organization of Sec14L6. **b** Pull-down assays demonstrated that the CRAL-TRIO domain and CT of Sec14L6 was co-pelleted with purified His-ACSL3 Δ TM in vitro from 3 independent experiments. The Coomassie blue staining of proteins used in the assay was shown on the bottom. **c** Representative images of live BODIPY (magenta)-labeled HeLa cells transiently transfected with GFP-Sec14L6 truncations (green; the NT, the CRAL-TRIO and the CT region) and ACSL3-Halo (magenta) with insets under OA stimulation from at least 3 independent experiments. **d** Representative images of live BODIPY (blue)-stained HeLa cells transiently transfected with GFP-Sec14L6 deletion mutants (green; Δ NT, Δ CRAL-TRIO and Δ CT region) and ACSL3-Halo (magenta) with insets under OA stimulation from at least 3 independent experiments. **e** AlphaFold-predicted structure of the CRAL-TRIO domain of Sec14L6 with secondary structures labeled in different color. **f** GFP-Trap

assays demonstrated interactions between GFP-Sec14L6 truncation mutants lacking of these secondary structures as in (e) and endogenous ACSL3 from 3 independent experiments. **g** Domain organization of ACSL3. **h** Representative images of live BODIPY (blue)-stained HeLa cells transiently transfected with GFP-Sec14L6 (green) and ACSL3-Halo deletion mutants (magenta; Δ NT, Δ AMP binding and Δ CT region) with insets under OA stimulation from at least 3 independent experiments. **i** GFP-Trap assays demonstrated ACSL3-NT preferentially interacted with Sec14L6-CRAL-TRIO domain from 3 independent experiments. **j** GST pull-down assays demonstrated that the CRAL-TRIO domain of Sec14L6 was co-pelleted with purified His-ACSL3- Δ TM, His-ACSL3-NT and His-ACSL3-CT in vitro from 3 independent experiments. The Coomassie blue staining of proteins used in the assay was shown on the right. Scale bar, 10 μ m in the whole cell images and 2 μ m in the insets in (c, d, h).



had any effect on the liposome association of GST-Sec14L6- Δ CRAL-TRIO (Fig. 4i). Together, these findings indicated that the CRAL-TRIO, but not full-length Sec14L6, can target membranes, and that ACSL3 stimulates the membrane association of full-length Sec14L6.

Since the AH was not located in the region required for interaction with ACSL3 (Fig. 3e, f), we therefore speculate that ACSL3 may trigger conformational changes of Sec14L6 to release the self-inhibitory configuration. To test this idea, we performed fluorescence resonance energy transfer (FRET) assays to monitor Sec14L6 conformational changes as previously reported⁴¹. We fused the fluorescent proteins Clover and mRuby2 to the N and C termini of Sec14L6, respectively,

and collected the fluorescent signals from Clover-Sec14L6-mRuby2 in HeLa cells (Fig. 4m). Importantly, at LD regions with Halo-ACSL3 enrichment, normalized FRET signals decreased significantly compared to other regions without Halo-ACSL3 enrichments (Fig. 4n, o). These results indicate that ACSL3 binding caused an increase in the distance between Clover and mRuby2, highlighting a potential role of ACSL3 in the release of the Sec14L6 self-inhibitory conformation.

PGRMC1 recruits Sec14L6 to the ER

As a potential lipid transporter involved in LD formation, Sec14L6 is likely associated with the ER. To investigate whether and how Sec14L6

Fig. 4 | The CRAL-TRIO domain of Sec14L6 targets LD via an AH.

a Representative images of live BODIPY (magenta)-stained HeLa cells transiently expressing GFP-Sec14L6 truncations (green; the NT, the CRAL-TRIO and the CT region) under OA stimulation from at least 3 independent experiments. **b** Representative images of live HeLa cells transiently expressing GFP-Sec14L6-CRAL-TRIO upon scrambled or ACSL3 siRNAs treatments under OA stimulation from at least 3 independent experiments. **c** Immunoblots showing the efficiency of ACSL3 siRNAs used in **(b)** from 3 independent experiments. Schematic representation of an AH in the CRAL-TRIO domain of Sec14L6 with a point mutation C135E **(d)** that would impair the AH **(e)**. **f** AlphaFold-predicted structure of the CRAL-TRIO domain of Sec14L6 showing the C135E (cyan) in the AH (magenta). **g** Representative images of live HeLa cells transiently expressing GFP-Sec14L6-CRAL-TRIO and GFP-Sec14L6-CRAL-TRIO-C135E under OA stimulation from at least 3 independent experiments. **h, i** Liposome pelleting assays showing His-Sec14L6-CRAL-TRIO (0.25 μ M), but not His-Sec14L6- Δ CRAL-TRIO (0.25 μ M), was co-pelleted with sucrose-loaded liposomes from 3 independent experiments. S, supernatant; P,

pellet. **j, k** Liposome pelleting assays showing the addition of His-ACSL3 Δ TM (0.25 μ M) and His-ACSL3-NT Δ TM (0.25 μ M), but not His-ACSL3-CT (0.25 μ M), promotes the membrane association of GST-Sec14L6 (0.25 μ M) from 3 independent experiments. **l** As in **(k)**, the addition of His-ACSL3 Δ TM (0.25 μ M) or the two ACSL3 truncations (0.25 μ M for each mutant) had no effect on the membrane association of GST-Sec14L6 Δ CRAL-TRIO from 3 independent experiments. **m** Schematic diagram of Clover-Sec14L6-mRuby2 protein. **n** Confocal images showing live HeLa cells transiently expressing Clover-Sec14L6-mRuby2 along with ACSL3-Halo with insets on the bottom from 3 independent experiments. Normalized FRET signal is indicated by a pseudocolored image. **o** Normalized FRET signal from either ACSL3/Sec14L6 co-enriched regions or other cells without substantial co-enrichments in HeLa cells in 3 independent experiments. Each dot represents one normalized FRET signal ratio from one region. Two-tailed unpaired Student's *t* test. Mean \pm SD. Scale bar, 10 μ m in the whole cell images and 2 μ m in the insets in **(a, b, g & n)**.

recognizes the ER, we performed mass spectrometry (MS) to identify proteins on the ER that interact with Sec14L6, which led to the identification of PGRMC1 (Fig. 5a and Supplementary Data 1). PGRMC1 is a component of a progesterone-binding protein complex⁴² and has been reported to play a role in heme homeostasis⁴³ and cholesterol synthesis⁴⁴. CoIP assays performed in the Sec14L6-GFP-KI line confirmed that Sec14L6 interacted with PGRMC1 at endogenous levels (Fig. 5b).

Next, we performed in vitro pull-down assays to investigate whether Sec14L6 binds to PGRMC1. In these assays, purified GST-Sec14L6, but not the GST tag alone, bound to His-PGRMC1- Δ TM (Fig. 5c).

Importantly, live-cell imaging showed that cytosolic GFP-Sec14L6 was recruited to the ER marked by PGRMC1-Halo (Supplementary Fig. 5a), and OA treatment appeared to promote this recruitment (Fig. 5d vs Supplementary Fig. 5a). However, coIP assays showed that the Sec14L6-PGRMC1 interaction was not strongly affected by OA (Supplementary Fig. 5b), suggesting that OA may promote this recruitment in an indirect manner.

In addition, live-cell imaging confirmed that endogenous Sec14L6-GFP-KI could be recruited to the ER by PGRMC1-Halo (Fig. 5e), but not PGRMC2, a PGRMC1 homolog that is critical for adipocyte function⁴⁵ (Supplementary Fig. 5c). This suggests that Sec14L6 and PGRMC1 specifically interact.

We then investigated how Sec14L6 interacts with PGRMC1. Pull-down assays showed that the GOLD domain in the CT region of Sec14L6 bound to His-PGRMC1- Δ TM to a much greater extent than did the CRAL-TRIO or NT region (Fig. 5f). In line with this, live-cell imaging showed that deletion of the GOLD domain, but not the NT or CRAL-TRIO domain, abolished the association with PGRMC1 (Fig. 5g), indicating that the GOLD domain is required for interaction with PGRMC1, consistent with a role for the GOLD domain of other Sec14 proteins in mediating protein-protein interactions⁴⁶.

PGRMC1 possesses a TM domain in its NT region and a cytochrome b5 heme-binding domain in its CT region (Fig. 5h). Deletion of the CT of PGRMC1, but not the NT (amino acids 45–72; the TM is retained), abolished the colocalization between PGRMC1 and Sec14L6 (Fig. 5i), indicating that the CT of PGRMC1 is required for Sec14L6 recruitment.

To further confirm this recruitment, we performed knock-down assays. Exploiting a specific interaction between RFP and the RFP nanobody (RFPnb), we ectopically targeted PGRMC1- Δ TM-RFPnb to the outer mitochondrial membrane (OMM) via Tom22-mCh (Fig. 5j). Remarkably, cytosolic GFP-Sec14L6 was strongly recruited to the OMMs that were positive for PGRMC1 (Fig. 5k, n). In contrast, GFP-Sec14L6 could not be recruited to the OMM by ACSL3 (Fig. 5l–n), suggesting that ACSL3 is not a recruitment factor for Sec14L6. These results suggest that PGRMC1 functions as an adaptor to recruit Sec14L6 to the ER.

We then investigated whether PGRMC1 is required for targeting Sec14L6 to the ER. Subcellular fractionation showed that the suppression of PGRMC1 by siRNAs significantly reduced the level of Sec14L6 in the ER fractions of Sec14L6-GFP-KI (Fig. 5o, p) or HeLa cells transiently expressing GFP-Sec14L6 (Supplementary Fig. 5d). Notably, the residual ER localization of GFP-Sec14L6 in PGRMC1 knockdown cells suggests other unknown factors could act as alternative adaptors for Sec14L6 in the absence of PGRMC1. In addition, PGRMC1 was not required for the LD targeting of Sec14L6, as live-cell images showed that PGRMC1 depletion did not abolish the LD localization of Sec14L6 in the Sec14L6-GFP-KI line (Supplementary Fig. 5e). These results support that PGRMC1 is a key, though perhaps not exclusive, factor required for the ER targeting of Sec14L6.

Sec14L6 deficiency impairs PIP homeostasis of LDs and the ER

Next, we sought to explore how Sec14L6 promotes LD formation. Sec14L6 belongs to the Sec14 protein family of PITPs, which have been shown to transfer lipids such as PI and PC (Sec14p in the yeast)²³ and PIP (such as PI4P for zebrafish Sec14L3)³¹. We hypothesized that Sec14L6 may regulate the lipid composition of LD and the ER to promote LD biogenesis. We therefore analyzed lipid species in LD or ER fractions by targeted lipidomics with relative quantitation. The purity of the ER and LD fractions was rigorously examined by Western blots (Fig. 6a and Supplementary Fig. 5f).

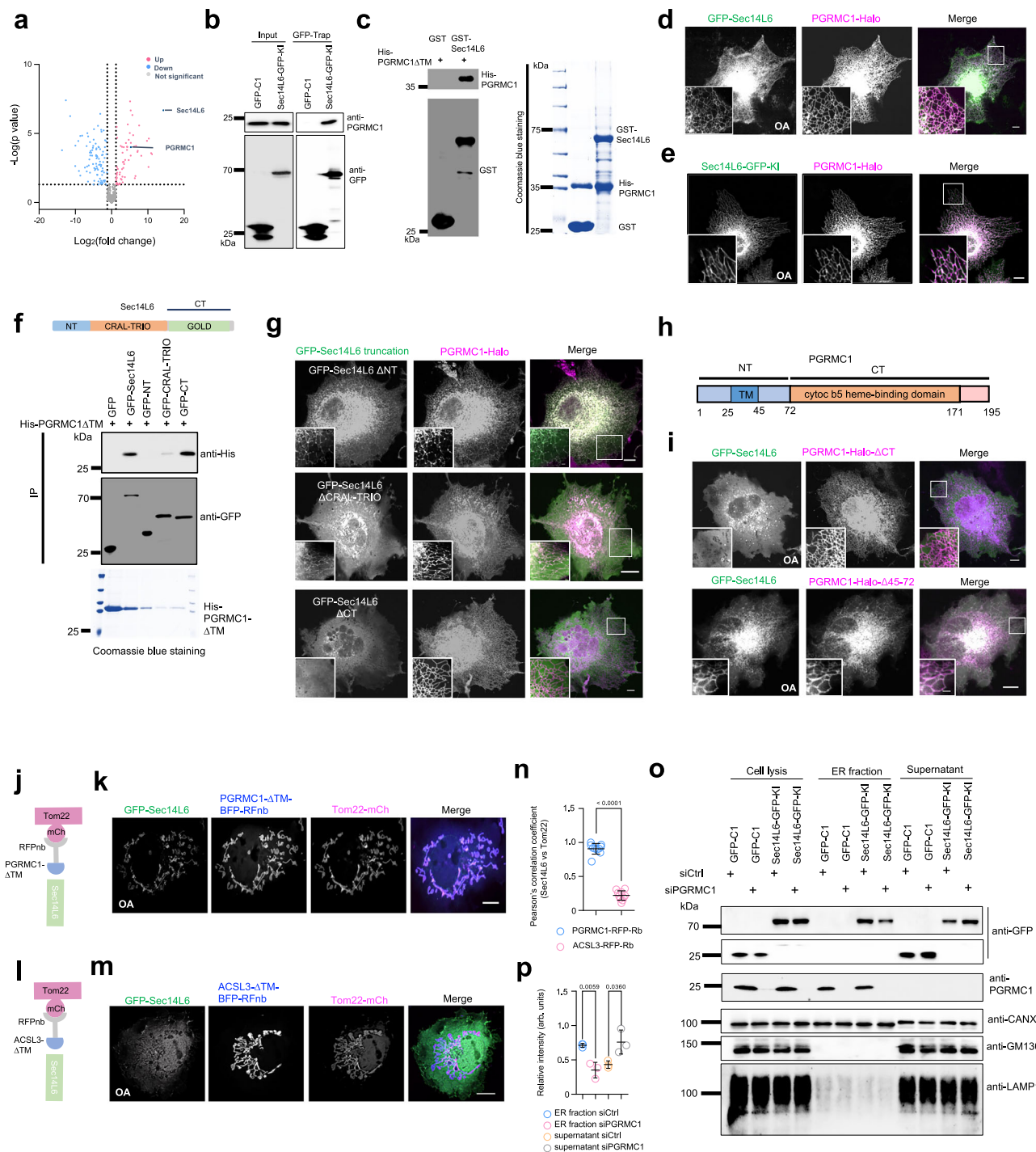
Analysis of LDs in Sec14L6 KO cells revealed strong increases in levels of PIPs (Fig. 6b), with PI4P (Fig. 6c) and PI(4,5)P₂ (Fig. 6d) showing the most pronounced accumulation. The LD levels of other PIPs including PI(3,5)P₂ and PI3P remained unaltered upon Sec14L6 depletion (Fig. 6b). In addition, levels of PE, PA, PI and PC in LDs remained largely unchanged in the LD fraction of Sec14L6 KO cells, except for a mild reduction in PS levels (Fig. 6e–g).

As ER lipid homeostasis is critical for LD biogenesis^{7,36,47,48}, we also examined the lipid composition in ER fractions. We observed significantly reduced levels of PI4P (Fig. 6h, i) and PI(4,5)P₂ (Fig. 6h, j) from Sec14L6 KO cells compared to controls in ER fractions. In addition, PE, PA and PC levels remained largely unchanged in Sec14L6 KO ER fractions (Fig. 6k, l). PS (Fig. 6k, m) and PI (Fig. 6k, n) levels were modestly elevated in the ER of Sec14L6 KO cells.

To confirm the results, we performed dot blots to examine PI4P levels in the ER or LD fractions using PI4P antibodies, as previously reported⁴⁹. Consistent with lipidomic data, dot blot assays showed that Sec14L6 deficiency caused an increase in PI4P level in the LD fraction but a decrease in the ER fraction, though the PI4P level of whole cell lysates was not strongly affected by Sec14L6 KO (Fig. 6o).

Sec14L6 preferentially transfers PI4P and PI(4,5)P₂ in vitro

Next, we investigated whether Sec14L6 directly transfer these PIPs using a fluorescence-based assay, as previously described³¹. Briefly, for



the measurement of PI4P transfer activities, donor liposomes containing DOPC, liver PE, DGS-NTA and PI4P were mixed with “heavy” (sucrose-loaded) acceptor liposomes containing DOPC, liver PE and DGS-NTA (Fig. 7a), and measurements were initiated after the addition of purified His-Sec14L6, His-CRAL-TRIO domain, His-Sec14L6- Δ CRAL-TRIO or His-GST (negative control). GST-tagged PH domain of FAPP conjugated with NBD moiety (NBD-FAPP-PH-GST) was used to detect PI4P in heavy liposomes. The size distribution of liposomes were confirmed by particle tracking analysis, and no spontaneous fusion or hemifusion of liposomes occurred (Supplementary Fig. 5g). Liposome pelleting assays confirmed that the FAPP-PH-GST bound specifically to donor (with PI4P) but not to acceptor (without PI4P) liposomes (Supplementary Fig. 5h).

In this assay, we found that PI4P transfer from donor to acceptor liposomes was accompanied by a strong increase in NBD fluorescence of heavy liposomes compared with that in the control (Fig. 7b), suggesting that Sec14L6 efficiently transfers PI4P *in vitro*. His-CRAL-TRIO showed a higher PI4P transfer rate than that of the full-length protein (Fig. 7b).

Given that alpha-tocopherol transfer protein, another protein belonging to the Sec14 family, can bind $\text{PI}(4,5)\text{P}_2$, as well as a strong effect on $\text{PI}(4,5)\text{P}_2$ distribution by Sec14L6 deficiency (Fig. 6), we therefore investigated whether Sec14L6 transfers $\text{PI}(4,5)\text{P}_2$ using the assay mentioned above except for the usage of NBD-PLC δ -PH as a $\text{PI}(4,5)\text{P}_2$ probe (Fig. 7a). Both His-Sec14L6 and His-CRAL-TRIO induced strong increase in NBD fluorescence compared to the control, with His-

Fig. 5 | PGRMC1 recruits Sec14L6 to the ER. **a** Volcano plot of protein candidates colPed with GFP-Sec14L6 in HEK293 cells compared with protein candidates colPed with GFP tag only. After removal of proteins that colPed with GFP tag, candidates that were considered significant ($-\log [P \text{ value}] > 1.3$; $P < 0.05$) were labeled in orange ($\text{Log}_2 [\text{fold change}] > 0$; increased in abundance) or blue ($\text{Log}_2 [\text{fold change}] < 0$; decreased in abundance) from 3 independent experiments. **b** GFP-Trap assays demonstrated interactions between endogenous Sec14L6-GFP-KI and endogenous PGRMC1 from 3 independent experiments. **c** GST pull-down assays demonstrated that purified GST-Sec14L6, but not GST tag, was pelleted with purified His-PGRMC1 in vitro from 3 independent experiments. The Coomassie blue staining of proteins used in the assay was shown on the right. **d** Representative images of a live HeLa cells transiently transfected with GFP-Sec14L6 (green) and PGRMC1-Halo (magenta) with one boxed region on the bottom upon OA treatments from at least 3 independent experiments. **e** Representative images of live BODIPY-stained Sec14L6-GFP-KI (green) cells transiently transfected with PGRMC1-Halo (magenta) in presence of OA loading with insets from at least 3 independent experiments. **f** Pull-down assays demonstrated that the CT of Sec14L6 was pelleted with purified His-PGRMC1 in vitro from 3 independent experiments. The Coomassie blue staining of proteins used in the assay was shown on the bottom. **g** Representative images of live HeLa cells transiently transfected with indicated GFP-Sec14L6 truncations (green) and PGRMC1-Halo (magenta) with insets upon OA treatments from at least 3 independent experiments. **h** Domain organization of

PGRMC1. **i** Representative images of live HeLa cells transiently transfected with GFP-Sec14L6 (green) and indicated PGRMC1-Halo truncations (magenta) with insets upon OA treatments from at least 3 independent experiments. **j** Schematic cartoon of RFPnb-mediated recruitment of PGRMC1-BFP-RFnb to the outer mitochondrial membranes (Tom22-mCh) in presence of GFP-Sec14L6. **k** Representative images of a HeLa cell expressing PGRMC1-BFP-RFnb (blue), GFP-Sec14L6 (green) and Tom22-mCh (magenta) from at least 3 independent experiments. **l** Schematic cartoon of RFPnb-mediated recruitment of ACSL3-BFP-RFnb to the outer mitochondrial membranes (Tom22-mCh) in presence of GFP-Sec14L6. **m** Representative images of a HeLa cell expressing ACSL3-BFP-RFnb (blue), GFP-Sec14L6 (green) and Tom22-mCh (magenta) from at least 3 independent experiments. **n** Pearson's correlation coefficient of GFP-Sec14L6 colocalized with Tom22-mCh either in presence of PGRMC1-BFP-RFnb (10 cells) or ACSL3-BFP-RFnb (10 cells). Each dot represents a value of Pearson's correlation coefficient of a cell. More than 3 independent experiments. Two-tailed unpaired Student's *t* test. Mean \pm SD. **o** Immunoblots showed the level of Sec14L6-GFP-KI in ER membrane fractions of either control or PGRMC1-depleted cells stably using GFP vector as a negative control from 3 independent experiments. **p** Ratio of Sec14L6-GFP-KI level of ER fractions between control and PGRMC1 depletion based on 3 independent assays. Two-tailed unpaired Student's *t* test. Mean \pm SD. Scale bar, 10 μm in the whole cell images and 2 μm in the insets in (**d**, **e**, **g**, **i**, **k** & **m**).

CRAL-TRIO being more efficient (Fig. 7c), indicating that Sec14L6 is able to transfer PI(4,5)P₂. Taken together, in vitro assays demonstrated that Sec14L6 can transfer PI4P and PI(4,5)P₂.

Liposome sedimentation assays (Fig. 7d) showed that purified His-Sec14L6 did not bind PC/PE liposomes (under 0% PI4P or 0% PI conditions; Fig. 7e, left), as shown in Fig. 4k. However, either the full-length or the His-CRAL-TRIO domain bound evidently to PI4P-containing liposomes (Fig. 7e), aligning with a robust PI4P transfer activity of Sec14L6. Binding to PI-containing liposomes was substantially weaker, detectable only at very high PI concentrations (~10 mol%) (Fig. 7e, left). These results indicate Sec14L6's preference for PI4P over PI.

In addition, Sec14L6 did not transfer NBD-PC, NBD-PE, or NBD-PA, but exhibited low transfer activity for NBD-PS in vitro (Fig. 7f-j). A FRET-based assay⁵¹ confirmed a slow, time-dependent increase in NBD-PS fluorescence after Sec14L6 addition, plateauing at ~90 min (Supplementary Fig. 5i-k). No significant increase occurred with NBD-PA, NBD-PC, or NBD-cholesterol/Rho-PE (Supplementary Fig. 5l-n). Dithionite controls⁵² ruled out fluorescence artifacts from liposome fusion (Supplementary Fig. 5o). Thus, Sec14L6 transfers PI4P, PI(4,5)P₂, and PS (to a lesser extent) in vitro.

Lipid transfer activity of Sec14L6 contributes to LD biogenesis

Sec14L6 lacked PC transfer activity, indicating divergence in ligand-binding specificity between human Sec14L6 and yeast Sec14p. Supporting this, sequence alignment revealed that two residues critical for PC binding in Sec14p (S173 and T175)²³ are not conserved in human Sec14L proteins (Fig. 8a). Specifically, these positions correspond to nonpolar residues in Sec14L6 (I149 and A151, respectively), suggesting an evolutionary loss of PC-binding capacity. In contrast, the PI-binding related residues of Sec14p (R65 and T236)²³ are conserved in Sec14L6 (R45 and T213) (Fig. 8a, b). Notably, although the other residues involved in PI binding in Sec14p such as E207 and K239 are also conserved in Sec14L6 (E184; K216), K66 (S46 in Sec14L6) is not conserved (Fig. 8a). This may explain the minimal binding between Sec14L6 and PI in vitro.

Notably, we found that a PI-binding defective mutant (R45A, T213D) of Sec14L6, as previously described by Schaaf et al.²³, impaired the binding of His-Sec14L6 with PI4P (Fig. 8c, d) or PI(4,5)P₂ (Fig. 8e), as well as the transfer of these two PIPs (Fig. 8f, g). Notably, the binding affinity of Sec14L6 to PI4P was higher than that to PI(4,5)P₂ (Fig. 8c, e), consistent with a higher PI4P transfer activity compared to PI(4,5)P₂ (Figs. 7b, c and 8f, g). These results indicated that the two residues

(R45A and T213D) of Sec14L6 are essential for the transfer of PI4P and PI(4,5)P₂.

Importantly, functional assays revealed that this Sec14L6 mutant failed to rescue the LD formation defect (Fig. 8h). In contrast, expression of either WT or another point mutant (A151I) that targets a residue corresponding to the PC binding site (T175) in Sec14p significantly restored LD formation in Sec14L6 KO cells (Fig. 8h, i). These results suggest that transfer activity of Sec14L6 towards PIPs, but not PC, is important for LD biogenesis.

To further confirm the key role of lipid transfer activity of Sec14L6 in LD formation, we generated four space-filling mutants of Sec14L6, in which conserved hydrophobic residues in the CRAL-TRIO domain were mutated to tryptophan (79VV-80WW; 153F-W; 171L-W; 237L-W) (Fig. 8j). In vitro lipid transfer assay confirmed impaired lipid transfer activity in these mutants (Fig. 8k). Live-cell imaging demonstrated that the defect in LD formation was specific to Sec14L6, as reintroduction of WT Sec14L6 significantly rescued the phenotype (Fig. 8l). Notably, none of the four space-filling mutants effectively restored LD formation in Sec14L6 KO cells (Fig. 8l, m). Therefore, we conclude that the lipid transfer activity of Sec14L6 contributes to LD biogenesis.

Sec14L6 promotes the differentiation of adipose-derived mesenchymal stem cells

We next investigated the potential physiological functions of Sec14L6 in human adipose-derived mesenchymal stem cells (ADSCs)⁵³, which can differentiate into adipocytes after stimulation, with the formation of numerous LDs being a hallmark of mature adipocytes. Mature ADSCs were defined by the presence of visibly large LDs (>2 μm) marked by BODIPY and were further confirmed in bright field images. In the control, we observed that the number and size of LDs markedly increased after induction (up to 16 days) (Fig. 9a, g). Notably, we found that some giant LDs that were clearly seen in bright-field images at late timepoints (>10 days) were not efficiently stained with BODIPY (Fig. 9a). Therefore, we quantified the size or number of LDs using BODIPY and bright-field images. Suppression of Seipin or FTO, two factors that are essential for ADSC differentiation^{10,54}, almost completely blocked the formation of LDs (Fig. 9b, c, g). Notably, the suppression of Sec14L6 by siRNAs strongly impaired LD formation during differentiation after induction (Fig. 9d, g), to an extent similar to that of ACSL3 (Fig. 9e, g), but not as strongly as Seipin or FTO did. Interestingly, PGRMC1 (Fig. 9f, g), significantly reduced LD formation upon

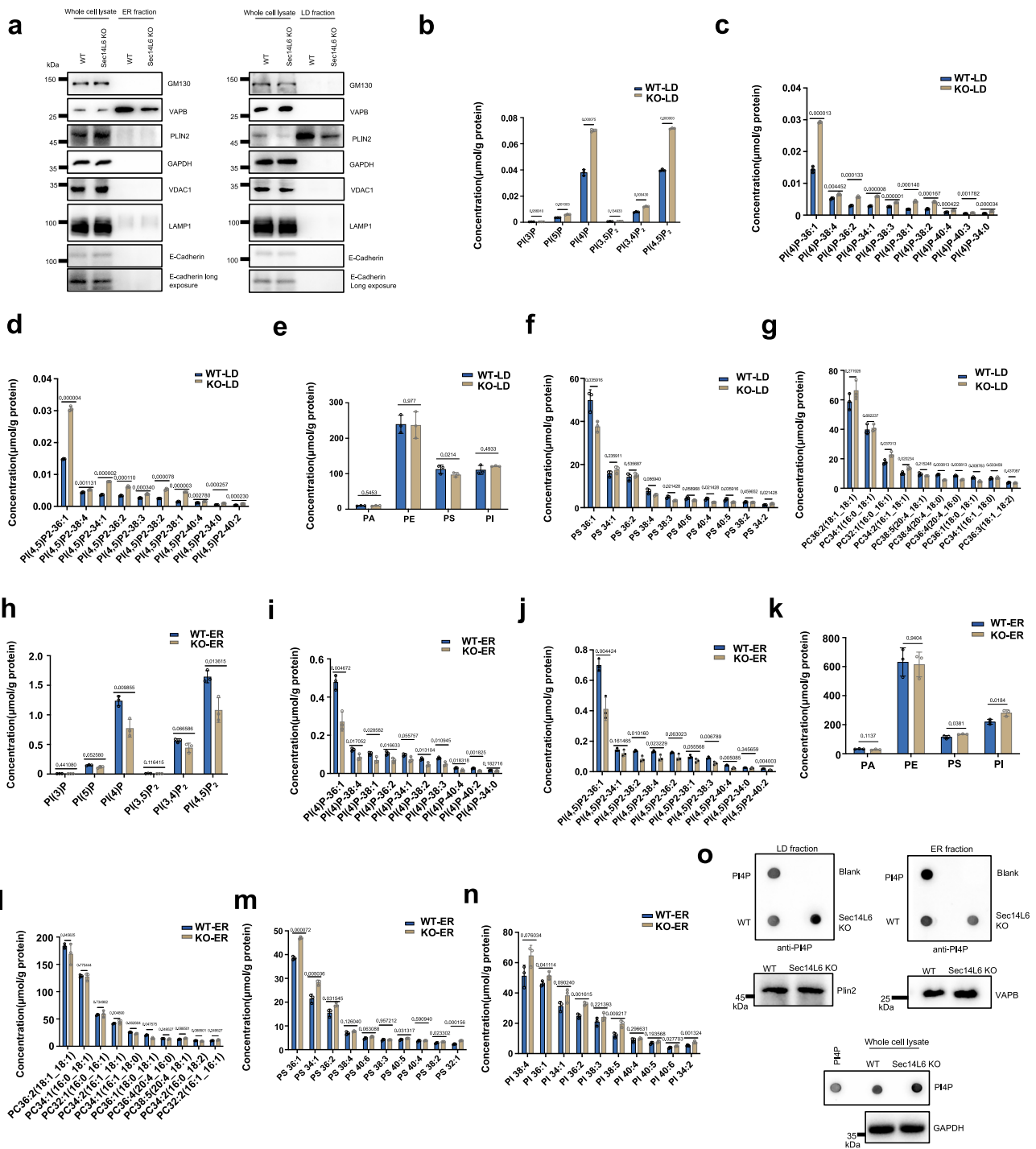


Fig. 6 | Sec14L6 deficiency impaired PIP homeostasis of the ER and LD.
a Membrane fractionation showing the purity of the ER or LD fractions used in the lipidomic analyses from at least 3 independent experiments. Western blots were performed with antibodies against Plin2 (LD marker), VAPB (ER marker), Lamp1 (late endosome/PM marker), E-cadherin (PM marker), VDAC1 (mitochondrial marker), GM130 (Golgi marker) and GAPDH (cytosol marker). The levels of PIPs (**b**), including PI4P (**c**) and PI(4,5)P₂ (**d**) in the LD fraction from control or Sec14L6 KO-2 HeLa cells from three biological replicates. In (**c**, **d**), top 10 lipid species based on abundance were shown. Two-tailed unpaired Student's *t* test. Mean ± SD. The levels of other glycerophospholipids (**e**), including PS (**f**) and PC (**g**) in the LD fraction from control or Sec14L6 KO-2 HeLa cells from three biological replicates. In (**f**, **g**), top 10 lipid species based on abundance were shown. Two-tailed unpaired

Student's *t* test. Mean ± SD. The levels of PIPs (**h**), including PI4P (**i**) and PI(4,5)P₂ (**j**) in the ER fraction from control or Sec14L6 KO-2 HeLa cells from three biological replicates. In (**i**, **j**), top 10 lipid species based on abundance were shown. Two-tailed unpaired Student's *t* test. Mean ± SD. The levels of other glycerophospholipids (**k**), including PC (**l**), PS (**m**) and PI (**n**) in the ER fraction from control or Sec14L6 KO-2 HeLa cells from three biological replicates. In (**l**, **m**, **n**), top 10 lipid species based on abundance were shown. Two-tailed unpaired Student's *t* test. Mean ± SD. **o** Representative dot blot assay showing cellular PI4P levels in the ER fraction (left panel), LD fractions (middle panel) or whole cell lysate (right panel) from WT or Sec14L6 KO-2 HeLa cells using PI4P antibody from 3 independent experiments. VAPB, Plin2 and GAPDH are used as the load control for the ER, LD or whole cell lysate, respectively, shown on the bottom.

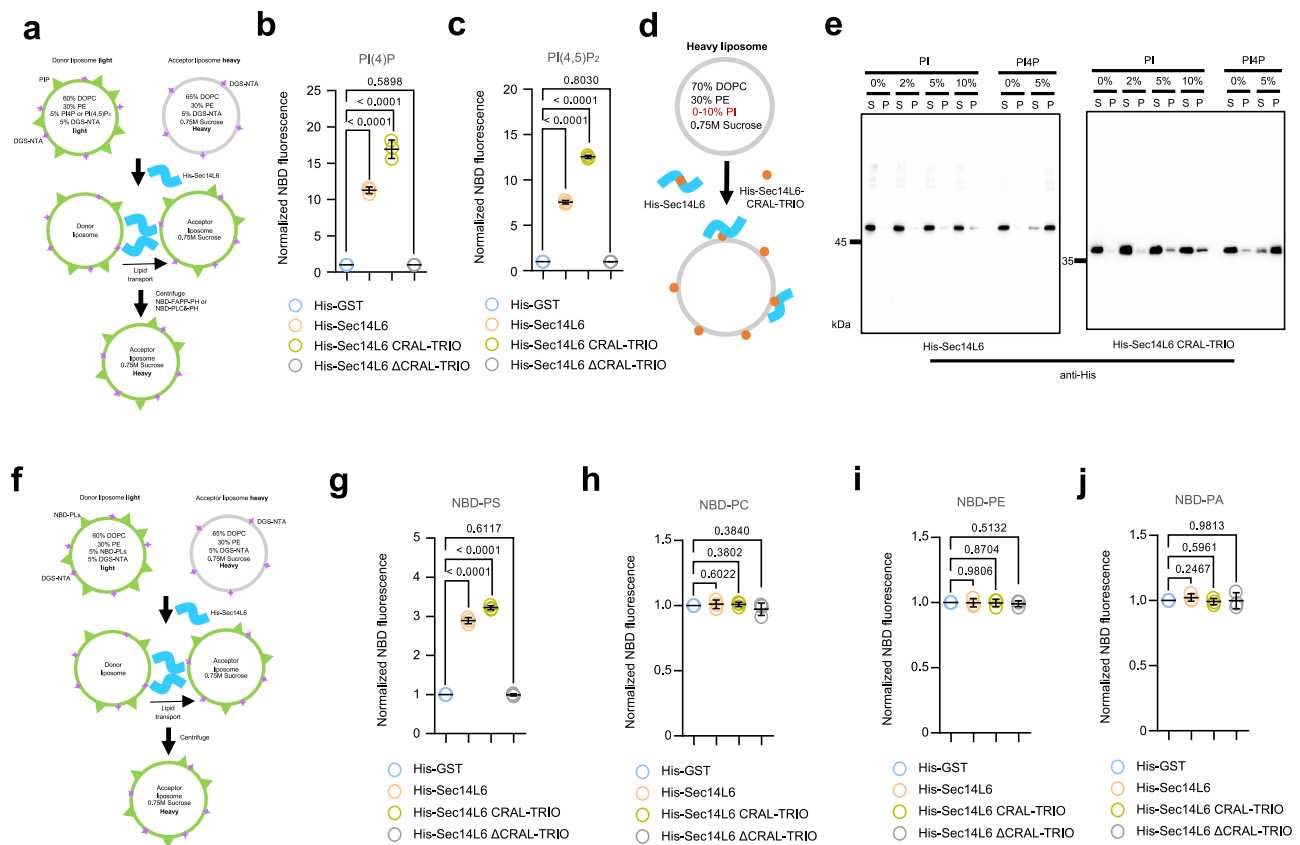


Fig. 7 | Sec14L6 preferentially transfers PI4P and PI(4,5)P₂ in vitro. **a** Schematic representation of indirect fluorescence-based in vitro lipid transfer assay of purified His-Sec14L6 using purified NBD-FAPP-PH or NBD-PLCδ-PH as a sensor for PI4P or PI(4,5)P₂, respectively. **b** Donor liposomes (light; 20 μM) containing lipids (5% PI4P, 5% DGS-NTA, 60% DOPC, and 30% PE) were mixed 1:1 with acceptor liposomes [heavy; 20 μM: 65% DOPC, 30% PE, and 5% DGS-NTA] in the presence of His-GST, His-Sec14L6, His-Sec14L6 CRAL-TRIO or His-Sec14L6-ΔCRAL-TRIO (0.25 μM for each). NBD-FAPP-PH was added to the heavy acceptor liposomes after reaction. The NBD fluorescence was normalized to the fluorescence intensity of His-GST ($n = 3$). Ordinary one-way ANOVA with Tukey's multiple comparisons test. Mean ± S.D. **c** As in (**b**), donor liposomes (light; 20 μM) containing fluorescent lipids [5% PI(4,5)P₂, 5% DGS-NTA, 60% DOPC, and 30% PE] were mixed 1:1 with acceptor liposomes [heavy; 20 μM: 65% DOPC, 30% PE, and 5% DGS-NTA] in the presence of His-GST, His-Sec14L6, His-Sec14L6 CRAL-TRIO or His-Sec14L6-ΔCRAL-TRIO (0.25 μM for each). NBD-PLCδ-PH was added to the heavy acceptor liposomes after reaction. The NBD

fluorescence was normalized to the fluorescence intensity of His-GST ($n = 3$). Ordinary one-way ANOVA with Tukey's multiple comparisons test. Mean ± S.D. **d** Schematic representation of liposome sedimentation assays. **e** Liposome sedimentation assays using liposomes containing PI (0, 2, 5, 10%) or PI4P (0, 5%) in the presence of His-Sec14L6 (0.25 μM) or His-Sec14L6-CRAL-TRIO (0.25 μM) from 3 independent experiments. His tag antibody was used in Western blots. S: supernatant; P: pellet. **f** Schematic representation of fluorescence-based in vitro lipid transfer assay. Donor liposomes (light; 20 μM) containing fluorescent lipids (2% NBD-PS (**g**), 2% NBD-PC (**h**), 2% NBD-PE (**i**) or 2% NBD-PA (**j**)) with 5% DGS-NTA, 63% DOPC, and 30% PE) were mixed 1:1 with acceptor liposomes [heavy; 20 μM: 65% DOPC, 30% PE, and 5% DGS-NTA] in the presence of His-GST, His-Sec14L6 proteins, His-Sec14L6 CRAL-TRIO or His-Sec14L6-ΔCRAL-TRIO (0.25 μM for each). The NBD fluorescence was normalized to the fluorescence intensity of His-GST ($n = 3$). Ordinary one-way ANOVA with Tukey's multiple comparisons test. Mean ± S.D.

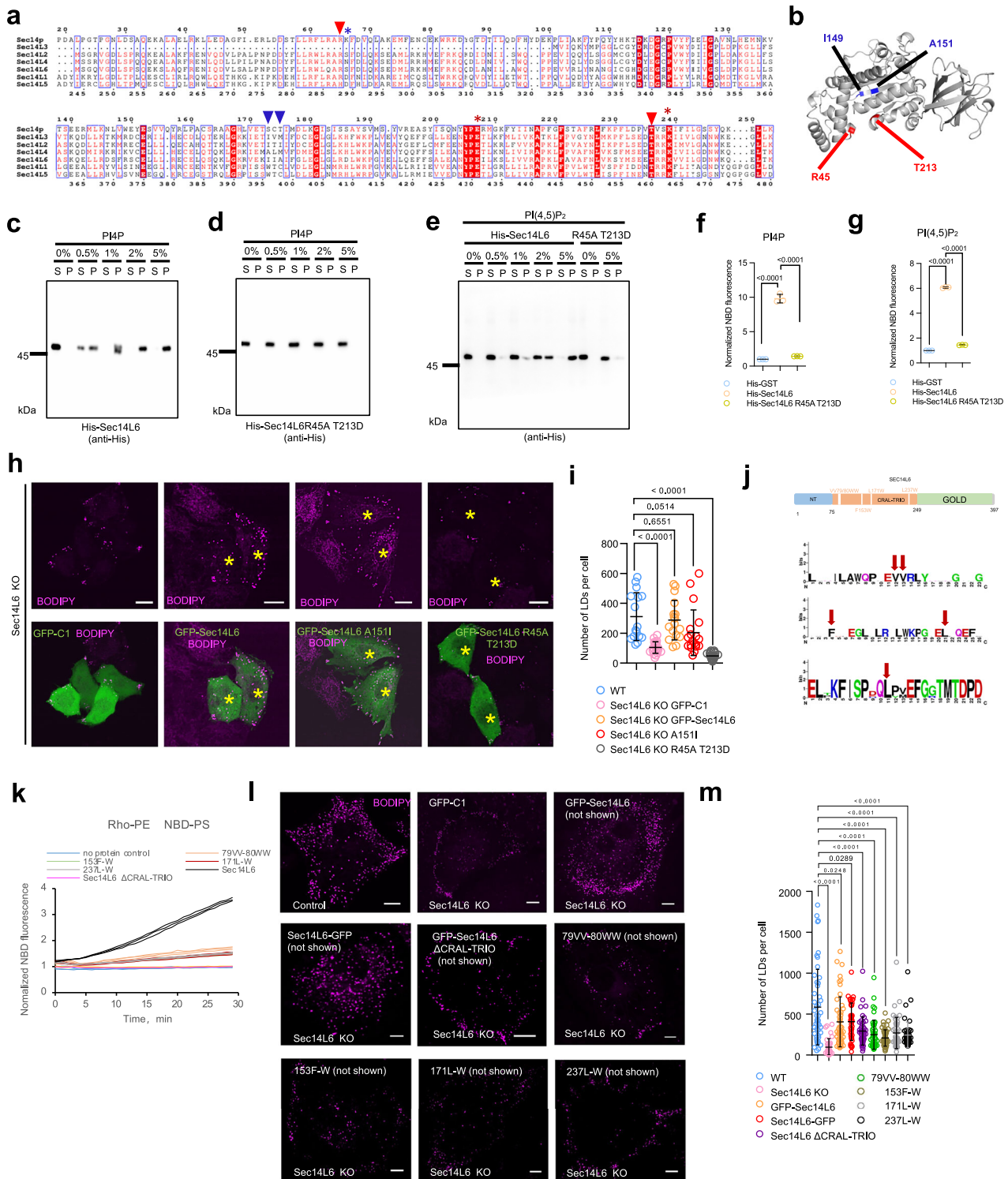
induction, supporting that PGRMC1 plays a role in LD biogenesis. The knockdown efficiency was confirmed using qPCR (Fig. 9h).

Next, we confirmed the role for Sec14L6 in ADSC differentiation by examining adipocyte-specific factors, such as adipisin⁵⁵, aP2⁵⁶, leptin⁵⁷, C-EBPα, and PPARγ using quantitative PCR⁵⁸. The findings showed that Seipin, FTO, and ACSL3 are essential for adipocyte differentiation, as their suppression led to significant reductions in the transcriptional levels of these factors (Fig. 9i–n). Notably, the mRNA levels of these factors were significantly reduced in Sec14L6- or PGRMC1-depleted cells (Fig. 9i–n), suggesting that Sec14L6 and PGRMC1 play important roles in this process. Taken together, our results demonstrate that Sec14L6 and its interactors ACSL3 and PGRMC1 play key roles in LD formation and are involved in ADSC differentiation.

Discussion

In this study, we identified Sec14L6 as a factor in the regulation of PIP homeostasis and biogenesis of LDs, which is important for the differentiation of adipose-derived mesenchymal stem cells. Our findings

reveal that Sec14L6 directly interacts with ACSL3, facilitating its association with LDs, and is recruited to the ER via the adaptor protein PGRMC1. Targeted lipidomics revealed that LDs from Sec14L6-KO cells exhibited aberrant accumulation of PI4P and PI(4,5)P₂, with a reduction of these PIPs within the ER compartment. In vitro lipid transfer assays demonstrated that Sec14L6 preferentially transports PI4P and PI(4,5)P₂, and also showed a low but significant transfer activity towards PS. Sec14L6 KO severely impaired nascent LD formation, a defect rescued by wild-type Sec14L6 but not by lipid-transfer-deficient mutants. Therefore, we propose that Sec14L6 regulates PIP homeostasis of LDs during LD biogenesis by transferring PI4P and PI(4,5)P₂ from LD surfaces to the ER (working model; Supplementary Fig. 6a, b). Notably, since the Sec14-like family can act as lipid metabolic sensors to regulate lipid homeostasis, our findings do not exclude another possibility: Sec14L6 may regulate PIP homeostasis by enhancing PI4P synthesis or its dephosphorylation during LD biogenesis. These two possibilities are not mutually exclusive. Sec14L6 deficiency impairs ER homeostasis and triggers ER stress (Supplementary Fig. 2a–c). Given the well-established coupling between ER homeostasis and LD



biogenesis, it remains challenging to determine whether the ER stress phenotype is a primary or secondary effect of Sec14L6 loss. As seen with other LD biogenesis factors like FIT2, the loss of Fit2 is also known to affect ER homeostasis³⁶. Therefore, Sec14L6 deficiency impairs lipid droplet biogenesis, at least in part, by disrupting ER homeostasis.

Emerging roles for PI4P in LD biology include its localization to LD surfaces^{32,59,60}, where it facilitates PS transfer from the ER³⁹ and promotes unilocaler LD formation during adipogenesis by recruiting adipocyte-specific CIDE proteins⁶¹. Our lipidomics analysis revealed low but detectable PI4P levels on LDs, and Sec14L6 deficiency caused PI4P accumulation on LDs, findings which align with these previous

studies and support the key role of PI4P in LD dynamics. In addition, PI(4,5)P₂ is detectable on LDs at levels comparable to PI4P. Lack of Lamp1 (a PM/late endosome marker) or E-Cadherin (PM marker) in the ER fraction (Fig. 6a, Supplementary Fig. 5f) indicates minimal contamination from these compartments, arguing against a PM origin for the observed PI(4,5)P₂. Sec14L6 KO also increases LD PI(4,5)P₂, suggesting that Sec14L6 transfers this lipid from LDs to the ER. Such transfer may regulate LD dynamics by either establishing PI(4,5)P₂ gradient or regulating effectors. Disrupted PI(4,5)P₂ homeostasis in KO cells may impair LD function, and the mechanism underlying this process warrants further investigation.

Fig. 8 | Lipid transfer activity of Sec14L6 is required for LD biogenesis.

a Sequence alignment between yeast Sec14p and human Sec14L1-6 with conserved residues highlighted in red. Red arrows denote two conserved residues (R45, T213) essential for PI binding; while blue arrows indicating two residues in yeast (S175, T177) for PC binding, which are not conserved in humans (I149, A151). Red asterisks label two conserved residues (E184; K216) while blue asterisk marks non-conserved residues (S46) in Sec14L6. **b** These four residues (R45, T213, I149, A151) as shown in **(a)** in the protein structure of Sec14L6 predicted by AlphaFold. **c, d** As in Fig. 7d, liposome sedimentation assays using liposomes containing PI4P (0, 0.5, 1, 2, 5%) in the presence of purified His-Sec14L6 (0.25 μ M; **c** or His-Sec14L6-R45A T213D (0.25 μ M; **d** from 3 independent experiments. His tag antibody was used in western blots. S: supernatant; P: pellet. **e** Liposome sedimentation assays using liposomes containing PI(4,5)P₂ (0, 0.5, 1, 2, 5%) in the presence of His-Sec14L6 (0.25 μ M) or His-Sec14L6-R45A T213D (0.25 μ M) from 3 independent experiments. His tag antibody was used in western blots. S: supernatant; P: pellet. **f** As in Fig. 7a, donor liposomes (light; 20 μ M) containing lipids (5% PI4P, 5% DGS-NTA, 60% DOPC, and 30% PE) were mixed 1:1 with acceptor liposomes [heavy; 20 μ M: 65% DOPC, 30% PE, and 5% DGS-NTA] in the presence of His-GST, His-Sec14L6 or His-Sec14L6-R45A T213D (0.25 μ M for each). NBD-FAPP-PH was added to the heavy acceptor liposomes after reaction. The NBD fluorescence was normalized to the fluorescence intensity of His-GST ($n = 3$). Ordinary one-way ANOVA with Tukey's multiple comparisons test. Mean \pm S.D. **g** Donor liposomes (light; 20 μ M) containing lipids (2% NBD-PS, 5% DGS-NTA, 63% DOPC, and 30% PE) were mixed 1:1 with acceptor liposomes [heavy; 20 μ M: 65% DOPC, 30% PE, and 5% DGS-NTA] in the presence of His-GST, His-

Sec14L6 or His-Sec14L6-R45A T213D (0.25 μ M for each). NBD-PLC δ -PH was added to the heavy acceptor liposomes after reaction. The NBD fluorescence was normalized to the fluorescence intensity of His-GST ($n = 3$). Ordinary one-way ANOVA with Tukey's multiple comparisons test. Mean \pm S.D. **h** Representative images of live BODIPY (magenta)-stained Sec14L6 KO-2 clones rescued with GFP empty vector, WT GFP-Sec14L6, GFP-Sec14L6-A151I or GFP-Sec14L6-R45A T213D. Yellow asterisks denote cells transfected with rescue constructs. The number of LDs in cells as shown in **(i)** in more than 3 independent experiments with at least 16 cells quantified per group. Ordinary one-way ANOVA with Tukey's multiple comparisons test. Mean \pm SD. **j** Schematic representation of conserved hydrophobic residues in the CRAL-TRIO domain of Sec14L6. **k** As in Supplementary Fig. 5g, donor liposomes (20 μ M) containing fluorescent lipids [2% NBD-PS, 2% Rhodamine-PE, 5% DGS-NTA, 61% DOPC, and 30% PE] were mixed 1:1 with acceptor liposomes [20 μ M: 65% DOPC, 30% PE, and 5% DGS-NTA] in the presence of either WT His-Sec14L6 (black), His-Sec14L6- Δ CRAL-TRIO, His-Sec14L6-VV79/80WW (orange), His-Sec14L6-F153W (green), His-Sec14L6-L171W (red) or His-Sec14L6-L237W (gray) (0.25 μ M for each). The NBD fluorescence was normalized to the fluorescence intensity at time = 0 ($n = 3$). **l** Representative images of live BODIPY (magenta)-stained control HeLa or Sec14L6 KO rescued with GFP empty vector, WT GFP-Sec14L6, Sec14L6-GFP, GFP-Sec14L6- Δ CRAL-TRIO, GFP-Sec14L6-VV79/80WW, GFP-Sec14L6-F153W, GFP-Sec14L6-L171W or GFP-Sec14L6-L237W from at least 3 independent experiments. **m** The number of LDs in cells as shown in **(l)** in more than 3 independent experiments with at least 36 cells quantified per group. Ordinary one-way ANOVA with Tukey's multiple comparisons test. Mean \pm SD. Scale bar, 10 μ m in **(h, l)**.

It should be noted that the PS distribution between LDs and the ER was mildly affected by Sec14L6 deficiency, accompanied by a low but significant transfer activity of Sec14L6 towards PS *in vitro*, suggesting a role for Sec14L6 in PS transfer in LD biogenesis. Given a potential link between the PIP and PS transfer events mediated by Sec14L6, future work should verify a role for Sec14L6 in PI4P/PS exchange between the ER and LD, reminiscent of the function of OSBP^{62,63} or ORP2/5/8^{39,64–66} at ER-trans-Golgi or -PM contacts.

ORP5 regulates LD morphology and dynamics at ER-associated membrane contacts^{38,39}. The loss of ORP5 results in PS deficiency and PI4P accumulation on LDs³⁹. While both Sec14L6 and ORP5 transfer lipids between the ER and LDs, they exhibit key differences. ORP5, a tail-anchored ER membrane protein, acting as a tether at membrane contact sites^{39,64}, regulates LD morphology likely post-detachment from the ER³⁹ and is conserved across metazoans. In contrast, Sec14L6 is cytosolic, lacks membrane anchors, and is exclusive to large mammals (e.g., absent in mice). Its ER/LD association depends on interacting partners (e.g., PGRMC1, ACSL3) rather than tethering at membrane contact sites. Notably, while ORP5 is present across eukaryotes, their role in LD biogenesis appears necessary but insufficient in cells of larger mammals due to a high demand in LD biogenesis in these cells. Functionally, compared to rodents with faster LD turnover, larger mammals exhibit higher lipid storage needs, necessitating redundant or specialized LD regulatory pathways. Sec14L6 likely evolved to complement ORP5/8 in managing lipid flux under conditions of enhanced LD biogenesis and maintenance (e.g., adipose tissue development in humans).

Genetic complementation assays suggest non-redundant roles for Sec14L6 and ORP5 (Supplementary Fig. 3a–d), indicating specialized functions. In yeast, Kes1p (an ORP homolog in mammals) antagonizes Pik1p (a PI4-kinase)-mediated PI4P synthesis on trans-Golgi, which is counteracted by Sec14p^{23,67,68}, indicating a functional cooperation among Sec14p, Kes1p/ORP and Pik1p/PI4K in PIP homeostasis and Golgi vesicle biogenesis. Whether this antagonism is conserved in human LD biogenesis remains unclear. Given the role of Sec14p in the activation of Pik1p, it is tempting to speculate that Sec14L6 or its partners (PGRMC1/ACSL3) may modulate the activities of PI4K or Sac1 to create PI4P-enriched microdomains for LD formation in humans. Future studies should explore interactions among Sec14L6 and its partners, as well as with ORP2/5, PI4-kinases, and Sac1 to unravel their regulatory network.

By analyzing lipids associating with affinity-tagged LTPs over-expressed in HEK293 cells, a recent study showed that Sec14L6 associated with PC and PE (Titeca et al. 2024, BioRxiv). However, our results showed that, unlike yeast Sec14p, Sec14L6 did not conserve PC-binding activity and could not transfer PC *in vitro*. Given the 'in cellulo' technique used in that study, the association of Sec14L6 with PC/PE in cells is likely context-dependent (e.g., mediated by membrane micro-environments or protein interactions) rather than reflecting direct transfer activity.

In addition to Sec14L6 and ORP5, multiple LTPs have also been localized to ER-LD interfaces, including ORP2¹⁷, VPS13A and VPS13C^{18,19}, and ATG2⁶⁹. These likely mediate context-specific lipid transfer (e.g., PC, PE, cholesterol) during LD formation, maturation, or stress adaptation. Delineating their spatial and temporal coordination will clarify their contributions to LD biology.

Dysregulated LD biogenesis underlies numerous disorders including type II diabetes, cancer, heart disease, and viral infections^{70,71}. Sec14L6's restriction to large mammals highlights an evolutionary divergence in LD regulation, offering insights into species-specific metabolic adaptations. Our work opens avenues for targeting Sec14L6-mediated lipid transport in disease contexts.

Methods

Cell culture, transfection, RNAi

Human cervical cancer HeLa cells (ATCC), human embryonic kidney 293T (ATCC), human hepatocellular carcinoma HepG2 (ATCC), human hepatoma Huh7 cells and mouse hepatocyte AML-12 cells were grown in (Invitrogen) supplemented with 10% fetal bovine serum (Gibco). All of the cell lines used in this study were confirmed free of mycoplasma contamination.

Transfection of plasmids and RNAi oligos was carried out with Lipofectamine 2000 and RNAi MAX, respectively. For transfection, cells were seeded at 4×10^5 cells per well in a six-well dish -16 h before transfection. Plasmid transfections were performed in OPTI-MEM (Invitrogen) with 2 μ l Lipofectamine 2000 per well for 6 h, followed by trypsinization and replating onto glass-bottom confocal dishes at 3.5×10^5 cells per well. Cells were imaged in live-cell medium (DMEM with 10% FBS and 20 mM Hepes with no penicillin or streptomycin) -16–24 h after transfection. For siRNA transfections, cells were plated on 3.5 cm dishes at 30–40% density, and 2 μ l Lipofectamine RNAimax (Invitrogen) and 50 ng siRNA were used per well. At 48 h after transfection, a

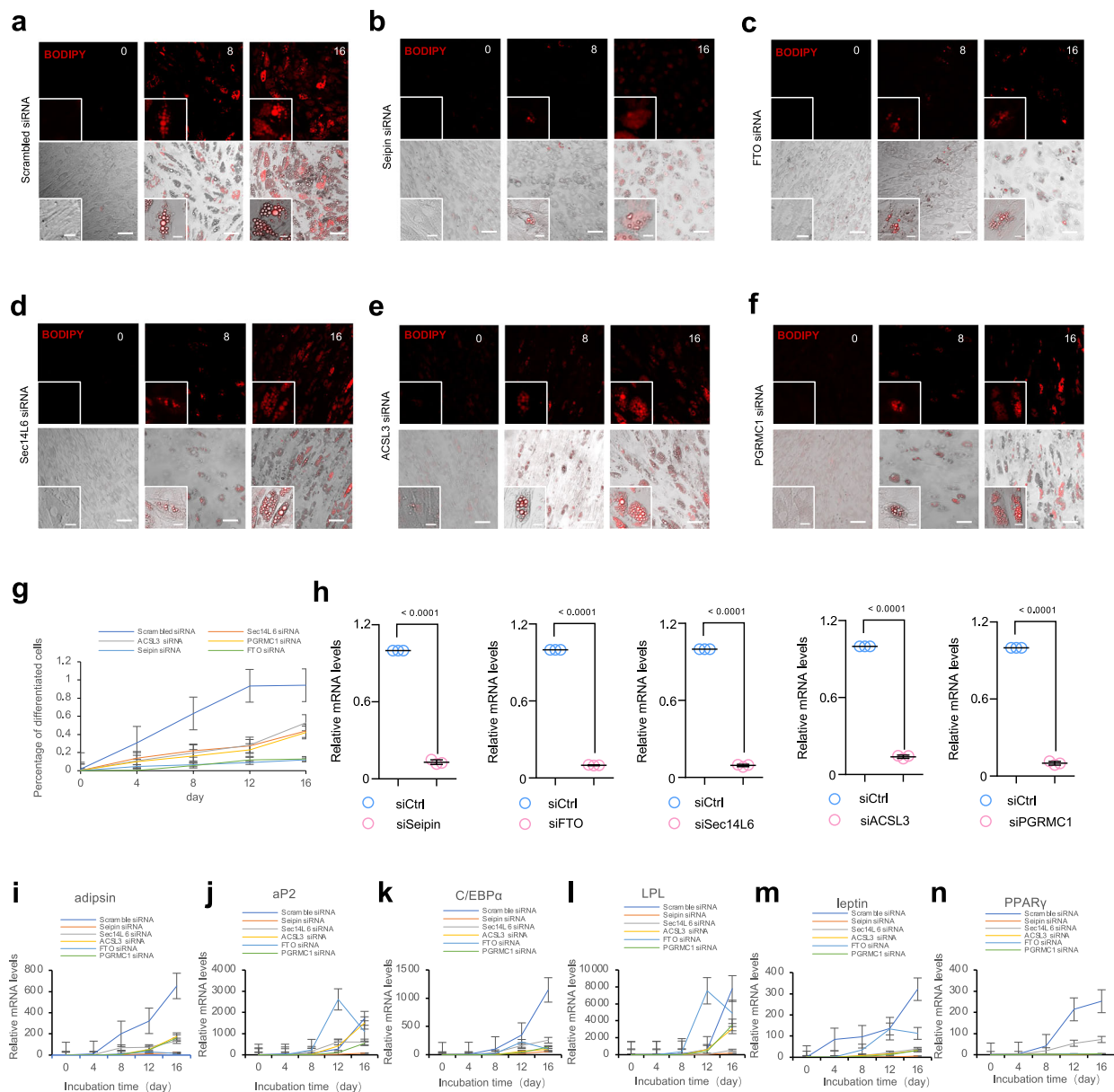


Fig. 9 | A role for Sec14L6 in differentiation of adipose stem cell differentiation. Representative images of live BODIPY (red)-stained ADSCs at time=0, 8, 16 day, treated with scrambled (a), Seipin (b), FTO (c), Sec14L6 (d), ACSL3 (e) or PGRMC1 (f) siRNAs from 3 independent experiments. Top panel: BODIPY channel; bottom panel: merged images of BODIPY and DIC channels with insets. **g** Percentage of mature ADSCs in (a–f) in 3 independent experiments. Mean \pm SD. Mature ADSCs were defined by the presence of visibly large LDs marked by BODIPY and were

further confirmed in bright field images. **h** qPCR showing the efficiency of suppression of Seipin, FTO, Sec14L6, ACSL3 and PGRMC1 in cells as in (a–f) from 3 independent experiments. Two-tailed unpaired Student's test. Mean \pm SD. qPCR showed the mRNA levels of factors in ADSC differentiation, including adipin (i), aP2 (j), C/EBP α (k), LPL (l), leptin (m) or PPAR γ (n), in 3 independent experiments. Mean \pm SD. Scale bar, 50 μ m in big area and 10 μ m in insets in (a–f).

second round of transfection was performed with 50 ng siRNAs. Cells were analyzed 24 h after the second transfection for suppression. The RNAi oligos for knockdown assays are listed in Supplementary Table 1.

CRISPR–Cas9-mediated gene editing

To make Sec14L6 KO HeLa cell lines, two gRNAs (5'-CTCCTGTGTATGCATCCAGG-3' and 5'-AACGGCATATGCGGCCACGA-3') were used to delete ~38 bp from exon 23 of Sec14L6 gene (Supplementary Fig. S1J). Complementary gRNAs were annealed and subcloned into the pSpCas9(BB)-2A-GFP (pX-458) vector (Addgene 48138) using BbsI. Upon transfection, HeLa cells were grown in an antibiotic-free medium for 48 h, followed by single-cell sorting by fluorescence-based flow cytometry.

To make Sec14L6-GFP-KI HeLa cell lines, a single gRNA (5'-GAAATTCTAGGTGAACCTCA-3') were used to target the N-terminus of the Sec14L6 gene (Supplementary Fig. S4C). HeLa cells were transfected with plasmids encoding the gRNA and a donor construct containing sGFP and two homologous arms using Lipofectamine 2000. 48 h after transfection, single clones were sorted by flow cytometry. A positive clone was verified by DNA gels (Supplementary Fig. S4D) and immunoblots (Supplementary Fig. S4E).

Plasmids

Sec14L6(NM_001193336), ACSL3(NM_203372.1), PGRMC1(NM_006667) were cloned from HeLa cDNA library. The coding sequence (CDS) of Sec14L6 and its truncation mutants were cloned into mEGFP-

C1(addgene 54579) between Sall and SacII. 14xHis-NEDD8-Sec14L6 was constructed by cloning its CDS to 14xHis-NEDD8 vector. The CDS of ACSL3, PGRMC1 and their truncation mutants were cloned into Halo-N1 (addgene 54767) using SacII and EcoRI. GST-Sec14L6 was constructed by cloning the Sec14L6 CDS into PGEX-2T vector using BamHI and EcoRI. 14xHis-NEDD8-PGRMC1 and 14xHis-NEDD8-ACSL3 were constructed by cloning the ORFs into 14xHis-NEDD8 vector using BamHI and HindIII. The FAPP-PH construct was a gift from Dr. Shunji Jia (Institute of Genetics and Developmental Biology, Chinese Academy of Sciences). The RFP-GFP-PLIN2 construct was a gift from Dr. Binbin Ding (Guangzhou Laboratory). The primers for plasmid construction are listed in Supplementary Table 2.

Western blotting

After being heated to 95 °C for 10 min, the SDS sample buffer was used to lyse the cells. The resulting samples were subjected to SDS-PAGE electrophoresis and transferred to a NC Transfer Membrane (HATF00010; Millipore). The membrane was then blocked with 5% (m/v) non-fat powdered milk at room temperature for 1 h and then incubated with primary antibodies at 4 °C overnight. After washing three times, membranes were incubated with secondary antibodies that were conjugated with horseradish peroxidase (1/10,000) for 1 h at room temperature. Visualization was performed using enhanced chemiluminescence (P0018M-2; Beyotime). The antibodies are listed in Supplementary Table 1.

Live imaging by high-resolution confocal microscopy

Cells were grown on 35 mm glass-bottom confocal MatTek dishes, and the dishes were loaded to a laser scanning confocal microscope (LSM900, Zeiss, Germany) equipped with multiple excitation lasers (405 nm, 458 nm, 488 nm, 514 nm, 561 nm and 633 nm) and a spectral fluorescence GaAsP array detector. Cells were imaged with the 63×1.4 NA iPlan-Apochromat 63× oil objective using the 405 nm laser for BFP, 488 nm for GFP, 561 nm for BODIPY-C12 558/568, tagRFP or mCherry and 633 nm for Janilia Fluo® 646 HaloTag® Ligand in a sequential line-scanning mode.

BODIPY-C12 558/568 staining in live cell

Cells were washed once with PBS, and was changed to complete medium containing 1 μM BODIPY-C12 558/568 and incubated at 37 °C for 20 min. Cells were washed with PBS three times and changed to imaging medium (DMEM supplemented with 10% FBS and 20 mM Hepes without phenol red) prior to imaging.

Halo staining in live cell

Cells were incubated with complete medium with 5 nM Janilia Fluo® 646 HaloTag® Ligand for 30 min. Cells were washed three times with complete medium to remove extra ligands, followed by incubation for another 30 min. Medium was replaced with imaging medium to remove unconjugated Halo ligands that has diffused out of the cells prior to imaging.

Purification of ER membranes by density gradient centrifugation

ER fractions were enriched using Endoplasmic Reticulum Isolation Kit (ERO100; Sigma-Aldrich) according to the manufacturer's instructions. Briefly, scrambled or PGRMC1 siRNA-treated HeLa cells stably expressing GFP empty vector or GFP-Sec14L6 from five confluent 10-cm dishes were collected, followed by centrifugation at 600 × *g* for 5 min. After washing the cells three times with PBS, the packed cell volume (PCV) was measured and then suspended in a volume of hypotonic extraction buffer (10 mM HEPES, pH 7.8, with 1 mM EGTA and 25 mM potassium chloride) equivalent to three times the PCV. After the incubation of the cells for 20 min at 4 °C allowing the cells to swell, the cells were centrifuged at 600 × *g* for 5 min, followed by the

measurement of the “new” PCV. After adding a volume of isotonic extraction buffer (10 mM HEPES, pH 7.8, with 0.25 M sucrose, 1 mM EGTA, and 25 mM potassium chloride) equivalent to two times the “new” PCV, the suspension was then transferred to a 7-ml Dounce homogenizer, followed by the lysis of the cells with 10 strokes and then the centrifugation of the homogenate at 1000 × *g* for 10 min at 4 °C. After the transfer of the supernatant to another centrifuge tube, the supernatant was centrifuged at 12,000 × *g* for 15 min at 4 °C, followed by another centrifugation for 60 min at 100,000 × *g* at 4 °C. The pellet was the microsomal fraction and further verified by Western blots using anti-Calnexin antibody.

Isolation of LD fractions by density gradient centrifugation

Isolation of LD fractions from HeLa cells or Sec14L6-GFP-KI HeLa line was performed as previously reported⁷² with some modifications. Briefly, cells were washed and lysed on ice using a Potter-Elvehjem tissue homogenizer in Hypotonic lysis medium (HLM, 20 mM Tris-Cl, pH 7.4; 1 mM EDTA; Protease inhibitors). The cell lysates were centrifuged at 1000 × *g* for 10 min at 4 °C, followed by addition of 1/3 volume of ice-cold HLM containing 60% sucrose (final 20% sucrose) into the supernatant and the floating fat layer. After aggregates of LDs were finely and thoroughly dispersed, the sample was layered into the bottom of a 13.2-ml ultracentrifuge tube for an SW41Ti rotor. 5 mL ice-cold HLM containing 5% sucrose and 5 mL ice-cold HLM were sequentially layered over the sample, followed by centrifuge at 28,000 × *g* for 30 min at 4 °C. The LD fraction was then transferred to a microcentrifuge tube, and was centrifuged at -20,000 × *g* for 10 min at 4 °C. The LD fraction was resuspended in ice-cold HLM, followed by checking purity of the LD fraction by SDS-PAGE of solubilized proteins and immunoblotting.

De-lipidation and LD formation induction

Cell de-lipidation and LD formation induction were conducted as described previously¹¹. Briefly, cells were delipidated by culturing in serum-free medium supplemented with 5% lipoprotein-deficient serum (Sigma) for 60 h. LD formation was induced by adding 0.2 mM OA (final concentration) for the indicated times.

TAG measurement

The indicated HeLa cells cultured in 6-well plates were lysed in 1% Triton X-100, and cell extracts were used to measure the TAG content by Triglyceride Colorimetric Assay Kit based on glycerol phosphate oxidase-based assays (GPO-PAP method) (BioSino Bio) according to the manufacturer's instructions. Briefly, the total protein concentration of each sample was determined by BCA assay (Thermo Fisher), and reactions were monitored in microplate reader at optical density 510 nm.

GFP-trap assay

GFP trap (GTA-100; ChromoTek) was used for the detection of protein–protein interactions, and the GFP-Trap assays were performed according to the manufacturer's protocol. Briefly, after 24 h transfection with the indicated plasmids, cells were lysed in ice-cold lysis buffer (50 mM Tris-HCl, pH 7.5, 150 mM NaCl, 1 mM EDTA, 1% Triton X-100 and protease inhibitor cocktail). Lysates were centrifuged at 17,949 × *g* for 10 min at 4 °C and pellets were removed. Supernatants were incubated with GFP-Trap agarose beads for 1 h at 4 °C with gentle rocking. After washing four times with lysis buffer, beads were boiled with SDS sample buffer. Proteins of interest were analyzed by immunoblotting. 5% input was used in GFP traps unless otherwise indicated.

GST tag and his tag protein purification

GST and His constructs were transformed into Escherichia coli BL21 (DE3) cells, and cells were incubated at 37 °C until the optical density (OD) at 600 nm reached 0.6–0.8. Subsequently, cells were incubated

at 16 °C for another hour, followed by induction with 1 mM IPTG overnight at 16 °C. Cells were lysed via sonication. GST fusion proteins were purified via the GST-tag Protein Purification kit (C600031-0025, Sangon, China), His fusion proteins were purified via the Ni-NTA Sefinose (TM) Resin Purification kit (G600033-0100, Sangon, China)

In vitro pull-down assays of GFP tag and his tag

HEK293 cells transiently transfected with GFP-Sec14L6 (full length and truncations) were lysed in high-salt lysis buffer (RIPA buffer containing 500 mM NaCl, proteasome inhibitors and PMSF). GFP-Trap beads were used to pellet GFP-Sec14L6 (full-length and truncations) from cell lysates, followed by washing with high-salt lysis buffer for 10 times. The GFP beads were incubated with Purified His-ACSL3 or His-PGRMC1 overnight at 4 °C, respectively, followed by washing beads with freshly prepared HNM buffer (20 mM Hepes, pH 7.4, 0.1 M NaCl, 5 mM MgCl₂, 1 mM DTT and 0.2% NP-40). GFP beads were resuspended in 100 μ L 2 \times SDS-sampling buffer. Re-suspended beads were boiled for 10 min at 95 °C to dissociate protein complexes from beads. Western blotting was performed using anti-GFP, ACSL3 or PGRMC1 antibodies. The Coomassie staining was performed for purified His-ACSL3 and His-PGRMC1.

Measurements of LD number and size

The LD number per HeLa or ADSC was counted manually with the help of an plugin of ImageJ (L54i; NIH), Cell Counter. In TEM images, the LD size was quantified by manually measuring the area of individual LD assisted by the “measure” tool in ImageJ.

ACSL3 activity measurement

The activity of ACSL3 was measured using the Amplex Red Acetyl-Coenzyme A Synthetase Assay Kit (S0391, Beyotime) according to the manufacturer’s instructions. Briefly, HeLa cells cultured in 6-well plates were lysed in BeyoLysis™ Buffer A for Metabolic Assay on ice for 10 min, followed by centrifugation at 12,000 $\times g$ for 5 min at 4 °C to obtain clear cell lysates. The total protein concentration of each sample was determined using the BCA Protein Assay Kit (Thermo Fisher Scientific). The Amplex Red reaction solution was prepared by mixing 42 μ L of ACS assay buffer, 2 μ L of Amplex Red, 2 μ L of enzyme solution, 2 μ L of substrate, and 2 μ L of enhancers. 50 μ L of the cell lysate was added to a 96-well plate, followed by the addition of 50 μ L of the prepared Amplex Red reaction solution. The plate was incubated at 37 °C for 30 min. Fluorescence intensity was measured using a microplate reader with excitation and emission wavelengths set at 560 nm and 590 nm, respectively. A standard curve was generated using the provided ACS standard solution, and the ACSL3 enzyme activity in the samples was calculated based on the standard curve. The enzyme activity was normalized to the total protein concentration of the samples. All experiments were performed in triplicate, and the results are presented as mean \pm standard deviation (SD).

Transmission electron microscopy

Control or Sec14L6 KO HeLa cells were fixed with 2.5% glutaraldehyde in 0.1 M Phosphate buffer, pH7.4 for 2 h at room temperature. After washing three times with 0.1 M Phosphate buffer, cells were scraped and collected with 0.1 M phosphate buffer followed by centrifugation at 956 $\times g$. The pellet was resuspended in PBS (0.1 M), and centrifuged at 956 $\times g$ for 10 min. This step was repeated three times. The samples were post-fixed with pre-cold 1% OsO₄ in 0.1 M Phosphate buffer for 2–3 h at 4 °C, followed by rinsing with PBS 3 times (3 \times 20 min). The samples were dehydrated in graded ethanol (50%, 70%, 85%, 90%, 95%, 2 \times 100%) with 15 min for each condition. The penetrations were performed in an order of acetone-epoxy (2:1); acetone-epoxy (1:1); epoxy. Each round of penetration was performed at 37 °C for 12 h. The samples were embedded in epoxy resin using standard protocols⁷³. Sections parallel to the cellular monolayer were obtained using a Leica

EM UC7 with the thickness of 60–100 nm and examined under Tecnai G2 20 TWIN (FEI) with accelerating voltage 200 kv. LDs and mitochondria were identified based on their respective morphology and were traced by hand. The number and size (area) of LDs were measured using the “measure” tool in ImageJ (NIH).

FRET

HeLa cells transiently transfected with Clover-Sec14L6-mRuby2 and ACSL3-Halo were imaged using a Dragonfly confocal microscopy system (Andor) equipped with a 60 \times N.A. 1.4 oil-immersion objective. Clover, mRuby2, and FRET fluorescence was collected with the following parameters: Clover: 488 nm excitation, 521 \pm 19 nm emission; mRuby2: 561 nm excitation, 594 \pm 21.5 nm emission; FRET: 488 nm excitation, 617 \pm 39.5 nm emission. Image analysis was performed with Matlab7.0 software to calculate N_{FRET} (Normalized FRET) according to the equation as previously described⁷⁴: $N_{FRET} = (I_{DA} - a_{IAA} - d_{IDD} / \sqrt{I_{DD} \times I_{AA}})$, where I_{DA} , I_{DD} , and I_{AA} are the background-subtracted FRET, Clover, and mRuby2 images, respectively.

Mass spectrometry for identification of GFP-Sec14L6-interacting Proteins

The identification of Sec14L6-interacting proteins by MS was described in our previous study⁷⁵. Briefly, the bound proteins were extracted from GFP-Trap agarose beads using SDT lysis buffer (4% SDS, 100 mM DTT, 100 mM Tris-HCl, pH 8.0), followed by sample boiling for 3 min and further ultrasonicated. Undissolved beads were removed by centrifugation at 16,000 $\times g$ for 15 min. The supernatant, containing proteins, was collected. Protein digestion was performed with the FASP method. Briefly, the detergent, DTT, and IAA in the UA buffer were added to block-reduced cysteine. Finally, the protein suspension was digested with 2 μ g trypsin (Promega) overnight at 37 °C. The peptide was collected by centrifugation at 16,000 $\times g$ for 15 min. The peptide was desalted with C18 StageTip for further LC-MS analysis. LC-MS/MS experiments were performed on a Q Exactive Plus mass spectrometer that was coupled to an Easy nLC (Thermo Fisher Scientific). The peptide was first loaded to a trap column (100 μ m \times 20 mm, 5 μ m, C18, Dr. Maisch GmbH) in buffer A (0.1% formic acid in water). Reverse-phase high-performance liquid chromatography (RP-HPLC) separation was performed using a self-packed column (75 μ m \times 150 mm; 3 μ m ReproSil-Pur C18 beads, 120 °A; Dr. Maisch GmbH, Ammerbuch) at a flow rate of 300 nl/min. The RP-HPLC mobile phase A was 0.1% formic acid in water and B was 0.1% formic acid in 95% acetonitrile. The gradient was set as follows: 2–4% buffer B from 0 to 2 min, 4–30% buffer B from 2 to 47 min, 30–45% buffer B from 47 to 52 min, 45–90% buffer B from 52 min and to 54 min, and 90% buffer B kept until to 60 min. MS data were acquired using a data-dependent top20 method dynamically choosing the most abundant precursor ions from the survey scan (350–1800 m/z) for HCD fragmentation. A lock mass of 445.120025 Da was used as the internal standard for mass calibration. The full MS scans were acquired at a resolution of 70,000 at m/z 200, and 17,500 at m/z 200. The maximum injection time was set to 50 ms for MS and 50 ms for MS/MS. Normalized collision energy was 27 and the isolation window was set to 1.6 Th. Dynamic exclusion duration was 60 s. The MS data were analyzed using Max Quant software version 1.6.1.0. MS data were searched against the UniProtKB human database (36,080 total entries, downloaded 2019.06.25). Trypsin was selected as the digestion enzyme. A maximum of two missed cleavage sites and a mass tolerance of 4.5 ppm for precursor ions and 20 ppm for fragment ions were defined for database search. Carbamidomethylation of cysteines was defined as a fixed modification, while acetylation of protein N-terminal and the oxidation of methionine were set as variable modifications for database searching. The database search results were filtered and exported with a <1% false discovery rate (FDR) at peptide-spectrum-matched level and protein level, respectively.

Protein expression and purification

The constructs were transfected into 30 × 10-cm dishes of HEK293T cells, and the medium was changed 5 h later. After another 24 h, cells were incubated in OptiMEM. The medium was collected 48 h later, and was centrifuged at 500 × *g* for 10 min. The supernatant was mixed with 500 μL of balanced HisPur™ Ni-NTA Resin (88221, Thermo Scientific) and incubated in a 4 °C shaking bed for 2 h. After centrifugation at 1000 × *g* for 10 min, the supernatant was discarded. Proteins on beads were washed with 20 mM Tris-HCl pH 8.0, 300 mM NaCl buffer containing 20 mM, 50 mM, 100 mM, and 200 mM imidazole sequentially. The eluted proteins were examined by Coomassie staining and western blotting. Then, the eluted proteins were concentrated (Millipore UFC900396), and washed with imidazole-free buffer to obtain the imidazole-free and concentrated His-Sec14L6 proteins.

Liposome pelleting assay

For liposome pelleting assays, proteins were diluted to ~7 μg/ml in osmotically matched protein dilution/HK buffer (20 mM Hepes, 120 mM NaCl, 1 mM EGTA, 0.2 mM CaCl₂, 1.5 mM MgCl₂, 1 mM DTT, 5 mM KCl, pH 7.4, 1% BSA) and were pre-cleared by ultracentrifugation at 120,000 *g* for 45 min using a TLA100.3 rotor in a Beckmann Optima-MAX benchtop ultracentrifuge. Heavy liposomes were prepared in the HK buffer with 0.75 M sucrose. 1 mL of pre-cleared protein solution was then mixed with 10 μL of the heavy liposomes and incubated with shaking at 25 °C for 15 min. Liposomes were recovered by ultracentrifugation (16,100 × *g* for 15 min), and supernatant and pellet fractions were resuspended in equal volumes of 1× Laemmli buffer and analyzed by western blots.

In vitro FRET-based lipid transfer assay

Lipid transfer assays shown in Fig. 7A–C were performed as follows. Light liposomes (DOPC: liver PE: PI4P/PI(4,5)P₂: DGS-NTA-Ni = 63: 30: 2: 5) were prepared in the HK buffer and coated with 500 μM NBD-PH protein. Heavy liposomes (DOPC: liver PE: DGS-NTA-Ni = 65: 30: 5, 0.75 M sucrose) were prepared in the HK buffer. The transfer reaction was initiated by mixing two liposome populations, with 0.25 μM proteins. After 15-min incubation at 25 °C, a cocktail of imidazole and proteinase K was added to terminate the transfer process, and the liposome suspensions were separated by centrifugation at 16,100 × *g* for 15 min. Heavy liposomes were collected and resuspend with 1 mL HK buffer, followed by centrifuge at 16,100 × *g* for 15 min. This step was repeated for three times. After three additional washes with HK buffer, heavy liposomes were incubated with NBD-FAPP-PH (for PI4P) or NBD-PLCδ-PH [for PI(4,5)P₂] for 15 min followed by three additional washes with HK buffer. Fluorescence signals were measured at 528 nm after excitation at 460 nm at 30 °C using a CLARIOstar Plus Microplate Reader (BMG LABTECH).

Lipid transfer assays shown in Fig. 7F–J were performed as follows. Light liposomes (DOPC: liver PE: NBD-PS/NBD-PC/NBD-PE/NBD-PA: DGS-NTA-Ni = 63: 30: 2: 5) were prepared in the HK buffer and coated with 500 μM NBD-PH protein. Heavy liposomes (DOPC: liver PE: DGS-NTA-Ni = 65: 30: 5, 0.75 M sucrose) were prepared in the HK buffer. The transfer reaction was initiated by mixing two liposome populations, with 0.25 μM proteins. After 15-min incubation at 25 °C, a cocktail of imidazole and proteinase K was added to terminate the transfer process, and the liposome suspensions were separated by centrifugation at 16,100 × *g* for 15 min. Heavy liposomes were collected and resuspend with 1 mL HK buffer, followed by centrifuge at 16,100 × *g* for 15 min. This step was repeated for three times. After three additional washes with HK buffer, heavy liposomes were collected for NBD signals measurement at 528 nm after excitation at 460 nm at 30 °C using a CLARIOstar Plus Microplate Reader (BMG LABTECH).

Lipid transfer assays shown in and Supplementary Fig. S5H–M were conducted according to the protocols described in previous

studies^{31,51}. Briefly, FRET-based lipid transfer reactions were performed in 100 μL volumes in 96-well plates containing a protein: lipid ratio of 1:800, with 0.25 μM proteins, 20 μM donor liposomes (61% DOPC, 30% liver PE, 2% NBD-PA/NBD-PS/NBD-PC/NBD-Cholesterol, 2% Rhodamine-PE, and 5% DGS-NTA-Ni) and 20 μM acceptor liposomes (65% DOPC, 30% liver PE and 5% DGS-NTA-Ni). The fluorescence intensity of NBD was measured via excitation at 460 nm and detection at 538 nm every 1 min for indicated time at 30 °C using a CLARIOstar Plus Microplate Reader. All data were normalized to the NBD fluorescence at first time point (*t* = 0).

Dithionite assay

After performing the lipid transfer reaction as shown Supplementary Fig. S5I, 2.5 μL freshly prepared dithionite buffer (100 mM dithionite in 50 mM Tris-HCl, pH = 10) was added to reactions, and NBD fluorescence was monitored for an additional 15 min.

Nanoparticle tracking analysis

The size distribution of liposomes was assessed by nanoparticle tracking analyses according to manufacturer instructions (NanoSight NS300, Malvern Panalytical). Briefly, the total number of particles was measured in light scatter mode without the use of an optical filter. Samples were applied with a constant flow rate using the supplied syringe-pump. Liposomes were diluted 1:100 in HK buffer (filtered with a 0.2 μm filter) prior to NTA measurements. Three to five videos of 60 s were recorded per sample with a sCMOS camera at 25 frames per second (1498 frames per video) and data were analyzed with the NTA software 3.1 (Build 3.1.54).

NBD-FAPP/PLCδ-PH

NBD-PH-FAPP molecular probes was prepared as previously described³¹. Briefly, after removing dithiothreitol, purified PH-FAPP or PH-PLCδ was mixed with a tenfold molar excess of N,N'-dimethyl-N-(iodoacetyl)-N'-(7-nitrobenz-2-oxa-1,3-diazol-4-yl) ethylenediamine (IANBD-amide, Molecular Probes). The labeling reaction was conducted overnight at 4 °C and terminated by adding a tenfold molar excess of L-cysteine. The free probe was removed by gel filtration and the labeled protein was analyzed by UV-visible spectroscopy to estimate labeling efficiency (~100%), which was calculated from the ratio of the optical density (OD) of tyrosine and tryptophan at 280 nm ($\epsilon = 29,450 \text{ M cm}^{-1}$ for PH-FAPP) and NBD at 495 nm ($\epsilon = 25,000 \text{ M cm}^{-1}$).

Targeted lipidomics with relative quantitation using LC-MS/MS

Lipid extraction. Lipids were extracted from approximately one million cells using a modified version of the Bligh and Dyer's method as described previously⁷⁶. Briefly, cells were homogenized in 750 μL of chloroform: methanol: MilliQ H₂O (3:6:1) (v/v/v). The homogenate was then incubated at 239 × *g* for 1 h at 4 °C. At the end of the incubation, 350 μL of deionized water and 250 μL of chloroform were added to induce phase separation. The samples were then centrifuged and the lower organic phase containing lipids was extracted into a clean tube. Lipid extraction was repeated once by adding 450 μL of chloroform to the remaining cells in aqueous phase, and the lipid extracts were pooled into a single tube and dried in the SpeedVac under OH mode. Samples were stored at –80 °C until further analysis. Upper aqueous phase and cell pellet were dried in a SpeedVac under H₂O mode. Total protein content was determined from the dried pellet using the Pierce® BCA Protein Assay Kit according to the manufacturer's protocol.

Lipidomics analyses. Lipidomic analyses were conducted at LipidALL Technologies using a ExionLC-AD coupled with Sciex QTRAP 6500 PLUS as reported previously⁷⁷. Separation of individual lipid classes of polar lipids by normal phase (NP)-HPLC was carried out using a TUP-HB silica

column (i.d. 150 × 2.1 mm, 3 μm) with the following conditions: mobile phase A (chloroform:methanol:ammonium hydroxide, 89.5:10:0.5) and mobile phase B (chloroform:methanol:ammonium hydroxide:water, 55:39:0.5:5.5). MRM transitions were set up for comparative analysis of various polar lipids. Individual lipid species were quantified by referencing to spiked internal standards. d₉-PC32:0(16:0/16:0), d₉-PC36:1p(18:0p/18:1), d₇-PE33:1(15:0/18:1), d₉-PE36:1p(18:0p/18:1), d₃₁-PS(d₃₁-16:0/18:1), d₇-PA33:1(15:0/18:1), d₇-PG33:1(15:0/18:1), d₇-PI33:1(15:0/18:1), C17-SL, d₅-CL72:8(18:2)4, d₇-LPE18:1, C17-LPI, C17-LPA, C17-LPS, C17-LPG were obtained from Avanti Polar Lipids. Free fatty acids were quantitated using d₃₁-16:0 (Sigma-Aldrich) and d₈-20:4 (Cayman Chemicals).

Analyses of PIPs were performed at LipidALL Technologies as previously described⁷⁸. Lipids were extracted under acidic conditions to increase recovery of phosphoinositides from biological tissues⁷⁹. In brief, cells were incubated with an extraction solvent containing chloroform:methanol (1:1) + 0.5 N HCl and 2 mM AlCl₃ for 10 min at 239 × g. Internal standard cocktail containing 17:0/20:4 PI3P, 17:0/20:4 PI4P, 17:0/20:4 PI5P, 17:0/20:4 PI(3,4)P2, 17:0/20:4 PI(3,5)P2, 17:0/20:4 PI(4,5)P2 and 17:0/20:4 PI(3,4,5)P3 from Avanti Polar Lipids was added into individual samples during extraction. At the end of incubation, deionized water was added to induce phase separation and the samples were centrifuged. The lower organic phase containing lipids were extracted and transferred to new tube. The extraction procedure was repeated for three rounds. Pooled extract was derivatised with 2 M TMS-diazomethane in hexane according to a published protocol⁷⁸ and analyzed on a Shimadzu Nexera 30-AD HPLC coupled with Sciex TRI-LE QUAD 6500 PLUS. PIPs were separated on a Daicel Chiralpak IB-U column (100 mm × 3.0 mm, 1.6 μm) using 10 mM ammonium formate in water as mobile phase A, and methanol as mobile phase B. Endogenous PIPs were quantitated by referencing to the levels of internal standards added.

Differentiation of human adipose-derived mesenchymal stem cells

Human adipose-derived mesenchymal stem cells were cultured to confluence before differentiation in a 24-well plate. For adipogenesis, the cells cultured in DMEM with 10% FBS were stimulated with a differentiation cocktail (Pricella PD-006, ProCell), which included 1-methyl-3-isobutylxanthine (IBMX), dexamethasone, human insulin and rosiglitazone in addition to penicillin-streptomycin, and glutamine (differentiation medium) for 3 days. Then the cells were cultured in medium containing a maintaining cocktail (Pricella PD-006, ProCell) including glutamine, penicillin-streptomycin and human insulin (maintaining medium) for 1 day and then cells were changed back to the differentiation medium. Cells were cultured in the two types of media alternately until sufficient LDs are visible in the stem cells. For imaging, cells at multiple differentiation timepoints (0, 8, 16 Days) were washed once with PBS, and was changed to complete medium containing 1 μM BODIPY-CL2 558/568 and incubated at 37 °C for 20 min. Cells were washed with PBS three times and changed to imaging medium (DMEM supplemented with 10% FBS and 20 mM Hepes without phenol red) prior to imaging by confocal and bright-field imaging.

Statistical analysis

All statistical analyses and *p*-value determinations were performed in GraphPad Prism8.0.1. All the error bars represent Mean ± SD. To determine *p*-values, ordinary one-way ANOVA with Tukey's multiple comparisons test was performed among multiple groups and a two-tailed unpaired Student's *t* test was performed between two groups.

Reporting summary

Further information on research design is available in the Nature Portfolio Reporting Summary linked to this article.

Data availability

The proteomics data generated in this study have been deposited into iProX under accession code PXD07027 [<https://www.iprox.cn/page/project.html?id=IPX0013812000>]. All the data and relevant materials, including reagents and primers, that supports the findings of this study are available from the corresponding author upon reasonable request. Source data are provided with this paper.

References

- Olzmann, J. A. & Carvalho, P. Dynamics and functions of lipid droplets. *Nat. Rev. Mol. Cell Biol.* **20**, 137–155 (2019).
- Zadoorian, A., Du, X. & Yang, H. Lipid droplet biogenesis and functions in health and disease. *Nat. Rev. Endocrinol.* **19**, 443–459 (2023).
- Thiam, A. R., Farese, R. V. Jr. & Walther, T. C. The biophysics and cell biology of lipid droplets. *Nat. Rev. Mol. Cell Biol.* **14**, 775–786 (2013).
- Yang, L. et al. The proteomics of lipid droplets: structure, dynamics, and functions of the organelle conserved from bacteria to humans. *J. Lipid Res.* **53**, 1245–1253 (2012).
- Welte, M. A. & Gould, A. P. Lipid droplet functions beyond energy storage. *Biochim. Biophys. Acta Mol. Cell Biol. Lipids* **1862**, 1260–1272 (2017).
- Moldavski, O. et al. Lipid droplets are essential for efficient clearance of cytosolic inclusion bodies. *Dev. Cell* **33**, 603–610 (2015).
- Joshi, A. S., Zhang, H. & Prinz, W. A. Organelle biogenesis in the endoplasmic reticulum. *Nat. Cell Biol.* **19**, 876–882 (2017).
- Thiam, A. R. & Ikonen, E. Lipid droplet nucleation. *Trends Cell Biol.* **31**, 108–118 (2021).
- Hugenroth, M. & Bohnert, M. Come a little bit closer! Lipid droplet-ER contact sites are getting crowded. *Biochim. Biophys. Acta Mol. Cell Res.* **1867**, 118603 (2020).
- Fei, W., Du, X. & Yang, H. Seipin, adipogenesis and lipid droplets. *Trends Endocrinol. Metab.* **22**, 204–210 (2011).
- Salo, V. T. et al. Seipin regulates ER-lipid droplet contacts and cargo delivery. *EMBO J.* **35**, 2699–2716 (2016).
- Wang, H. et al. Seipin is required for converting nascent to mature lipid droplets. *Elife* **5**, 16582 (2016).
- Harris, C. A. et al. DGAT enzymes are required for triacylglycerol synthesis and lipid droplets in adipocytes. *J. Lipid Res.* **52**, 657–667 (2011).
- Kassan, A. et al. Acyl-CoA synthetase 3 promotes lipid droplet biogenesis in ER microdomains. *J. Cell Biol.* **203**, 985–1001 (2013).
- Chen, F. et al. FIT2 organizes lipid droplet biogenesis with ER tubule-forming proteins and septins. *J. Cell Biol.* **220**, e201907183 (2021).
- Salo, V. T. & Ikonen, E. Moving out but keeping in touch: contacts between endoplasmic reticulum and lipid droplets. *Curr. Opin. Cell Biol.* **57**, 64–70 (2019).
- Hynynen, R. et al. OSBP-related protein 2 is a sterol receptor on lipid droplets that regulates the metabolism of neutral lipids. *J. Lipid Res.* **50**, 1305–1315 (2009).
- Kumar, N. et al. VPS13A and VPS13C are lipid transport proteins differentially localized at ER contact sites. *J. Cell Biol.* **217**, 3625–3639 (2018).
- Chen, S. et al. VPS13A and VPS13C influence lipid droplet abundance. *Contact Thousand Oaks* **5**, 25152564221125613 (2022).
- Wong, L. H., Gatta, A. T. & Levine, T. P. Lipid transfer proteins: the lipid commute via shuttles, bridges and tubes. *Nat. Rev. Mol. Cell Biol.* **20**, 85–101 (2019).
- Krahmer, N. et al. Phosphatidylcholine synthesis for lipid droplet expansion is mediated by localized activation of CTP:phosphocholine cytidyltransferase. *Cell Metab.* **14**, 504–515 (2011).
- Saito, K., Tautz, L. & Mustelin, T. The lipid-binding SEC14 domain. *Biochim. Biophys. Acta* **1771**, 719–726 (2007).

23. Schaaf, G. et al. Functional anatomy of phospholipid binding and regulation of phosphoinositide homeostasis by proteins of the sec14 superfamily. *Mol. Cell* **29**, 191–206 (2008).
24. Peterman, T. K., Ohol, Y. M., McReynolds, L. J. & Luna, E. J. Patellin1, a novel Sec14-like protein, localizes to the cell plate and binds phosphoinositides. *Plant Physiol.* **136**, 3080–3094 (2004).
25. Tejos, R. et al. PATELLINS are regulators of auxin-mediated PIN1 relocation and plant development in *Arabidopsis thaliana*. *J. Cell Sci.* **131**, jcs204198 (2018).
26. Montag, K., Ivanov, R. & Bauer, P. Role of SEC14-like phosphatidylinositol transfer proteins in membrane identity and dynamics. *Front. Plant Sci.* **14**, 1181031 (2023).
27. Costa, R. et al. SEC14L2, a lipid-binding protein, regulates HCV replication in culture with inter- and intra-genotype variations. *J. Hepatol.* **70**, 603–614 (2019).
28. Saeed, M. et al. SEC14L2 enables pan-genotype HCV replication in cell culture. *Nature* **524**, 471–475 (2015).
29. Gong, B. et al. The Sec14-like phosphatidylinositol transfer proteins Sec14L3/SEC14L2 act as GTPase proteins to mediate Wnt/Ca(2+) signaling. *Elife* **6**, 26362 (2017).
30. Gong, B. et al. Sec14L3 potentiates VEGFR2 signaling to regulate zebrafish vasculogenesis. *Nat. Commun.* **10**, 1606 (2019).
31. Gong, B. et al. A Golgi-derived vesicle potentiates PtdIns4P to PtdIns3P conversion for endosome fission. *Nat. Cell Biol.* **23**, 782–795 (2021).
32. Ren, J. et al. A phosphatidylinositol transfer protein integrates phosphoinositide signaling with lipid droplet metabolism to regulate a developmental program of nutrient stress-induced membrane biogenesis. *Mol. Biol. Cell* **25**, 712–727 (2014).
33. Diep, D. T. V. et al. A metabolically controlled contact site between vacuoles and lipid droplets in yeast. *Dev. Cell* **59**, 740–758 e710 (2024).
34. Eisenberg-Bord, M. et al. Identification of seipin-linked factors that act as determinants of a lipid droplet subpopulation. *J. Cell Biol.* **217**, 269–282 (2018).
35. Wang, H. et al. FITM2 deficiency results in ER lipid accumulation, ER stress, and reduced apolipoprotein B lipidation and VLDL triglyceride secretion in vitro and in mouse liver. *Mol. Metab.* **90**, 102048 (2024).
36. Becuwe, M. et al. FIT2 is an acyl-coenzyme A diphosphatase crucial for endoplasmic reticulum homeostasis. *J. Cell Biol.* **219**, e202006111 (2020).
37. Yuan, Z. et al. ATG14 targets lipid droplets and acts as an autophagic receptor for syntaxin18-regulated lipid droplet turnover. *Nat. Commun.* **15**, 631 (2024).
38. Guyard, V. et al. ORP5 and ORP8 orchestrate lipid droplet biogenesis and maintenance at ER-mitochondria contact sites. *J. Cell Biol.* **221**, e202112107 (2022).
39. Du, X. et al. ORP5 localizes to ER-lipid droplet contacts and regulates the level of PI(4)P on lipid droplets. *J. Cell Biol.* **219**, e201905162 (2020).
40. Zouiouich, M. et al. MOSPD2 is an endoplasmic reticulum-lipid droplet tether functioning in LD homeostasis. *J. Cell Biol.* **221**, e202110044 (2022).
41. Philipps, B., Hennecke, J. & Glockshuber, R. FRET-based in vivo screening for protein folding and increased protein stability. *J. Mol. Biol.* **327**, 239–249 (2003).
42. Ryu, C. S., Klein, K. & Zanger, U. M. Membrane associated progesterone receptors: promiscuous proteins with pleiotropic functions - focus on interactions with cytochromes P450. *Front. Pharm.* **8**, 159 (2017).
43. Piel, R. B. et al. A novel role for progesterone receptor membrane component 1 (PGRMC1): a partner and regulator of ferrochelatase. *Biochemistry* **55**, 5204–5217 (2016).
44. Rohe, H. J., Ahmed, I. S., Twist, K. E. & Craven, R. J. PGRMC1 (progesterone receptor membrane component 1): a targetable protein with multiple functions in steroid signaling, P450 activation and drug binding. *Pharm. Ther.* **121**, 14–19 (2009).
45. Galmozzi, A. et al. PGRMC2 is an intracellular haem chaperone critical for adipocyte function. *Nature* **576**, 138–142 (2019).
46. Anantharaman, V. & Aravind, L. The GOLD domain, a novel protein module involved in Golgi function and secretion. *Genome Biol.* **3**, research0023 (2002).
47. Choudhary, V. et al. Architecture of lipid droplets in endoplasmic reticulum is determined by phospholipid intrinsic curvature. *Curr. Biol.* **28**, 915–926 e919 (2018).
48. Gross, D. A., Zhan, C. & Silver, D. L. Direct binding of triglyceride to fat storage-inducing transmembrane proteins 1 and 2 is important for lipid droplet formation. *Proc. Natl Acad. Sci. USA* **108**, 19581–19586 (2011).
49. Du, Y. et al. Sec23IP recruits VPS13B/COH1 to ER exit site-Golgi interface for tubular ERGIC formation. *J. Cell Biol.* **223**, e202402083 (2024).
50. Kono, N. et al. Impaired alpha-TTP-PIPs interaction underlies familial vitamin E deficiency. *Science* **340**, 1106–1110 (2013).
51. Gao, Y., Xiong, J., Chu, Q.-Z. & Ji, W.-K. PDZD8 mediated lipid transfer at ER-LE/lys contacts is required for LE/lys positioning and neurite outgrowth. *J. Cell Sci.* **135**, jcs.255026 (2022).
52. Meers, P., Ali, S., Erukulla, R. & Janoff, A. S. Novel inner monolayer fusion assays reveal differential monolayer mixing associated with cation-dependent membrane fusion. *Biochim. Biophys. Acta* **1467**, 227–243 (2000).
53. Zhang, J. et al. Adipose-derived stem cells: current applications and future directions in the regeneration of multiple tissues. *Stem Cells Int.* **2020**, 8810813 (2020).
54. Merkesteyn, M. & Sellayah, D. Role of FTO in adipocyte development and function: recent insights. *Int. J. Endocrinol.* **2015**, 521381 (2015).
55. Cook, K. S. et al. Adipsin: a circulating serine protease homolog secreted by adipose tissue and sciatic nerve. *Science* **237**, 402–405 (1987).
56. Yu, G. et al. Adipogenic differentiation of adipose-derived stem cells. *Methods Mol. Biol.* **702**, 193–200 (2011).
57. Hwang, C. S., Loftus, T. M., Mandrup, S. & Lane, M. D. Adipocyte differentiation and leptin expression. *Annu. Rev. Cell Dev. Biol.* **13**, 231–259 (1997).
58. Clarke, S. L., Robinson, C. E. & Gimble, J. M. CAAT/enhancer binding proteins directly modulate transcription from the peroxisome proliferator-activated receptor gamma 2 promoter. *Biochem. Biophys. Res. Commun.* **240**, 99–103 (1997).
59. Han, L. et al. Lipid droplet-associated lncRNA LIPTER preserves cardiac lipid metabolism. *Nat. Cell Biol.* **25**, 1033–1046 (2023).
60. Kurokawa, Y. et al. Microautophagy in the yeast vacuole depends on the activities of phosphatidylinositol 4-kinases, Stt4p and Pik1p. *Biochim. Biophys. Acta Biomembr.* **1862**, 183416 (2020).
61. Wu, J. et al. PI(4)P recruits CIDE proteins to promote the formation of unilocular lipid droplets during adipogenesis and hepatic steatosis. *Proc. Natl Acad. Sci. USA* **122**, e2504219122 (2025).
62. Mesmin, B. et al. A four-step cycle driven by PI(4)P hydrolysis directs sterol/PI(4)P exchange by the ER-Golgi tether OSBP. *Cell* **155**, 830–843 (2013).
63. de Saint-Jean, M. et al. Osh4p exchanges sterols for phosphatidylinositol 4-phosphate between lipid bilayers. *J. Cell Biol.* **195**, 965–978 (2011).
64. Chung, J. et al. INTRACELLULAR TRANSPORT. PI4P/phosphatidylserine countertransport at ORP5- and ORP8-mediated ER-plasma membrane contacts. *Science* **349**, 428–432 (2015).

65. Moser von Filseck, J. et al. INTRACELLULAR TRANSPORT. Phosphatidylserine transport by ORP/Osh proteins is driven by phosphatidylinositol 4-phosphate. *Science* **349**, 432–436 (2015).
66. Wang, H. et al. ORP2 delivers cholesterol to the plasma membrane in exchange for phosphatidylinositol 4, 5-bisphosphate (PI(4,5)P(2)). *Mol. Cell* **73**, 458–473 e457 (2019).
67. Fang, M. et al. Kes1p shares homology with human oxysterol binding protein and participates in a novel regulatory pathway for yeast Golgi-derived transport vesicle biogenesis. *EMBO J.* **15**, 6447–6459 (1996).
68. Li, X. et al. Analysis of oxysterol binding protein homologue Kes1p function in regulation of Sec14p-dependent protein transport from the yeast Golgi complex. *J. Cell Biol.* **157**, 63–77 (2002).
69. Velikkakath, A. K., Nishimura, T., Oita, E., Ishihara, N. & Mizushima, N. Mammalian Atg2 proteins are essential for autophagosome formation and important for regulation of size and distribution of lipid droplets. *Mol. Biol. Cell* **23**, 896–909 (2012).
70. Gluchowski, N. L., Becuwe, M., Walther, T. C. & Farese, R. V. Jr. Lipid droplets and liver disease: from basic biology to clinical implications. *Nat. Rev. Gastroenterol. Hepatol.* **14**, 343–355 (2017).
71. Herker, E., Vieyres, G., Beller, M., Krahmer, N. & Bohnert, M. Lipid droplet contact sites in health and disease. *Trends Cell Biol.* **31**, 345–358 (2021).
72. Brasaemle, D. L. & Wolins, N. E. Isolation of lipid droplets from cells by density gradient centrifugation. *Curr. Protoc. Cell Biol.* **72**, 3 15 11–13 15 13 (2016).
73. Kumar, S., Ciraolo, G., Hinge, A. & Filippi, M. D. An efficient and reproducible process for transmission electron microscopy (TEM) of rare cell populations. *J. Immunol. Methods* **404**, 87–90 (2014).
74. Xia, Z. & Liu, Y. Reliable and global measurement of fluorescence resonance energy transfer using fluorescence microscopes. *Biophys. J.* **81**, 2395–2402 (2001).
75. Du, Y., Chang, W., Gao, L., Deng, L. & Ji, W.K. Tex2 is required for lysosomal functions at TMEM55-dependent ER membrane contact sites. *J. Cell Biol.* **222**, e202205133 (2023).
76. Song, J. W. et al. Omics-driven systems interrogation of metabolic dysregulation in COVID-19 pathogenesis. *Cell Metab.* **32**, 188–202 e185 (2020).
77. Lam, S. M. et al. A multi-omics investigation of the composition and function of extracellular vesicles along the temporal trajectory of COVID-19. *Nat. Metab.* **3**, 909–922 (2021).
78. Clark, J. et al. Quantification of PtdInsP3 molecular species in cells and tissues by mass spectrometry. *Nat. Methods* **8**, 267–272 (2011).
79. Boss, W. F. & Massel, M. O. Polyphosphoinositides are present in plant tissue culture cells. *Biochem. Biophys. Res. Commun.* **132**, 1018–1023 (1985).

Acknowledgements

We thank the School of Basic Medicine Innovation Research Center, Huazhong University of Science and Technology, for providing technical supports. We thank the Mass Spectrometry Core Facility of Shenzhen

Bay Laboratory for providing technical supports. W.J. was supported by National Natural Science Foundation of China (92354304; 32371343; 32570822) and Shenzhen Bay Scholars Program.

Author contributions

T. Zhou. and W. Ji. conceived the project and designed the experiments. T. Zhou, X. Hu, J. Xiong, Y. Du, A. Shi, W. Chang, L. Deng and J. Qin performed the experiments T. Zhou, X. Hu, Y. Du, J. Xiong, W. Chang, L. Deng and W. Ji. analyzed and interpreted the data. W. Ji. prepared the manuscript with inputs and approval from all authors.

Competing interests

The authors declare no competing interests.

Additional information

Supplementary information The online version contains supplementary material available at <https://doi.org/10.1038/s41467-025-65540-2>.

Correspondence and requests for materials should be addressed to Wei-Ke Ji.

Peer review information *Nature Communications* thanks Pingsheng Liu, and the other anonymous, reviewer(s) for their contribution to the peer review of this work. A peer review file is available

Reprints and permissions information is available at <http://www.nature.com/reprints>

Publisher's note Springer Nature remains neutral with regard to jurisdictional claims in published maps and institutional affiliations.

Open Access This article is licensed under a Creative Commons Attribution-NonCommercial-NoDerivatives 4.0 International License, which permits any non-commercial use, sharing, distribution and reproduction in any medium or format, as long as you give appropriate credit to the original author(s) and the source, provide a link to the Creative Commons licence, and indicate if you modified the licensed material. You do not have permission under this licence to share adapted material derived from this article or parts of it. The images or other third party material in this article are included in the article's Creative Commons licence, unless indicated otherwise in a credit line to the material. If material is not included in the article's Creative Commons licence and your intended use is not permitted by statutory regulation or exceeds the permitted use, you will need to obtain permission directly from the copyright holder. To view a copy of this licence, visit <http://creativecommons.org/licenses/by-nc-nd/4.0/>.

© The Author(s) 2025